Quantum speedup at zero temperature via coherent catalysis

Gabriel A. Durkin*

Uber Technologies, Inc., 1455 Market Street, Suite 400, San Francisco, California 94103, USA
and Berkeley Center for Quantum Information and Computation, University of California, Berkeley, California 94720, USA

(Received 12 October 2018; published 12 March 2019)

It is known that secondary nonstoquastic drivers may offer speedups or catalysis in some models of adiabatic quantum computation accompanying the more typical transverse field driver. Their combined intent is to raze potential barriers to zero during adiabatic evolution from a false vacuum to a true minimum; first-order phase transitions are softened into second-order transitions. We move beyond mean-field analysis to a fully quantum model of a spin ensemble undergoing adiabatic evolution in which the spins are mapped to a variable mass particle in a continuous one-dimensional potential. We demonstrate that the necessary criterion for enhanced mobility or "speedup" across potential barriers is actually a quantum form of the Rayleigh criterion. Quantum catalysis is exhibited in models where previously thought not possible, when barriers cannot be eliminated. For the 3-spin model with a secondary antiferromagnetic driver, catalyzed time complexity scales between linear and quadratic with the number of qubits. As a corollary, we identify a useful resonance criterion for quantum phase transition that differs from the classical one, but converges on it, in the thermodynamic limit.

DOI: 10.1103/PhysRevA.99.032315

I. INTRODUCTION

In computer science, computational tasks may be crudely divided into two categories: easy and hard. Easy problems are soluble in a time limit t^* that scales polynomially with n, the number of available computing resources (bits or qubits), $t^* \sim n^\alpha$, whereas hard tasks might take an exponentially long time to complete, $t^* \sim \alpha^n$. Much of the interest in *quantum* computing has been fueled by the possibility that classically hard problems can sometimes become "easy" when performed by a particular quantum algorithm running on a quantum computer.

One quantum computing paradigm particularly well suited to the solution of optimization problems is adiabatic quantum computing [1,2]. In this model, an ensemble of quantum bits (qubits) is initialized in the ground state of a trivial Hamiltonian. This could be, for instance, associated with a strong linear magnetic field. During the execution of the algorithm the Hamiltonian is smoothly and continuously changed or *annealed* into the "target" Hamiltonian encoding the original computational task. This ground state represents a globally optimal solution to that task. If the quantum annealing from initial to target Hamiltonian occurs sufficiently slowly or adiabatically, the system remains in the instantaneous ground state throughout, guaranteeing that the optimal solution is recovered in finite time. The system always stays at the lowest point on the energy surface or "cost function" landscape. This approach differs quite dramatically from classical approaches to optimization, possibly involving gradient descent techniques, where it can be impossible to know whether a recovered solution corresponds to a local or global minimum. This also assumes the cost function in parameter space is sufficiently smooth that gradient information can be derived—not often the case in combinatorial optimization.

While success is guaranteed in finite time by the adiabatic theorem [3], the energy landscape may become highly nontrivial during the annealing process; the ground state must navigate through a landscape of hills and valleys that spring up around it as the algorithm progresses. Large time penalties are suffered when energy barriers, of height $O(1)$ on the scale of the Hamiltonian, emerge between the current state of the system and the true minimum energy. These energy barriers are associated with a first-order phase transition during the adiabatic process. Under ideal circumstances the algorithm is executed at zero temperature, to preserve the system in its ground state, so there is no possibility of thermal activation over the barrier in question. The only remaining option is for the quantum state to tunnel through the barrier to the true ground state on the other side, exactly as first discussed by Gamow in his famous paper of 1928 describing α-particle decay [4]. The ground state is seen to jump in a discontinuous way between configurations, and the phase transition is described as "first order." This phenomenon is possibly the Achilles heel of quantum annealing: Tunneling, only possible via quantum mechanics, is also an exponentially slow process in w, the barrier width: $t^* \propto c^w$. Consequently, for problems which exhibit barrier widths scaling positively with system size n (number of qubits), the exponential delay in adiabatic passage at the phase transition produces an exponential slowdown in performance. This is reflected in an overall exponential-scaling time-to-solution with n. The problem instances that feature such first-order phase transitions seem to belong (unavoidably) to the class of "hard" problems [5].

In this paper, we will explore, in a fully quantum setting, techniques by which those barriers may be reduced, by the introduction of additional control fields or interactions. The idea that secondary control interactions might eliminate

*gabriel.durkin@uber.com

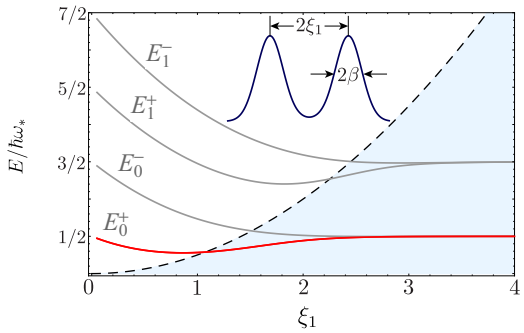

FIG. 1. Pairing of energies during transition from the unimodal to bimodal ground state. Here ξ_1 is a displacement variable and β a "width" variable. This important transition we call the quantum Rayleigh limit: $\xi_1 \sim \beta$, derived later in Eq. (5). As plotted, adjacent even and odd eigenvalues $E_k^{\pm}$ of the piecewise-parabolic potential are seen to "pair up," to become doubly degenerate, as the scaled separation of the wells increases beyond the order of the well widths, i.e., $\xi_1 \gg \beta$ (above for the case $\beta = 1$). In this limit (blue-shaded region) the energies are well below the barrier height (dashed line) and the intrapair spectral gap decreases exponentially with the barrier height V_0. A sketch of the ground-state wave function is shown (upper middle) in the limit of well-separated wells. For $\xi_1 < \beta$, violating the Rayleigh criterion, the wells coalesce and the vacuum energy E_0^+ (red) and other eigenenergies subsume the barrier. At the leftmost edge the two wells merge completely, and eigenvalues revert to those of a simple harmonic oscillator: $(n + 1/2)\hbar\omega$.

barriers, turning hard problems into easy ones, was proposed 16 years ago in Ref. [6], and the idea resurfaced more recently in Ref. [7] where the secondary driver was of a specific nonstoquastic type. Numerical support for quantum speedup in instances of spin glasses was given in Ref. [8].

Here we refer to controlled barrier suppression in a more general sense as "coherent catalysis." This invites a comparison with classical chemical kinematics in a sense that was perhaps first used for quantum information in Ref. [9] and that surfaced again recently in the context of adiabatic quantum computing in the excellent review by Albash and Lidar [10]. The application of the "catalyst" (secondary driver) during annealing lowers the activation energy of the migration from false to true ground state. The purity of the quantum state is preserved; hence the process is coherent.

We begin with an examination of a prototype double-well system, for which we establish the necessary conditions for a crossover from exponential to polynomial time complexity. This is associated with a qualitative change in the quantum ground state from a bimodal to unimodal profile, and energy level "unpairing," as illustrated in Fig. 1. An analogy is made with the Rayleigh diffraction limit of angular resolution in physical optics [11]. (Two pointlike objects are considered resolved when the maximum of one image coincides with the first minimum of the other. When applied to two Gaussian point-spread functions, the distance between the two maxima becomes comparable to the sum of their standard deviations.)

Moving to composite systems, we will see that the number n of adiabatically evolving qubits plays a nontrivial role in the time complexity; in some sense, quantum computers of mesoscopic scale might be better suited to certain classes of computational tasks, rather than holding fast to the naive idea that "more is simply better." Even in a completely decoherence-free setting the limit of large n will lead to a predominantly classical behavior. A peculiarity in our analysis produces an effective Planck's constant $\hbar$ that varies *inversely* with the number of qubits, attaining values much larger than 10^{-34} in systems of modest size (to be clarified in Sec. VII). As a result of this inverse relationship larger ensembles of qubits exhibit weaker quantum behavior.

The novelty of our technique is to move beyond a conventional "mean-field" calculation by inclusion of phenomena derived from or modified by the zero-point (vacuum) energy of the quantum system as it evolves through the shifting potential landscape. (In contrast, the mean-field description reproduces only that potential energy surface and ignores kinetic energy completely.) Even at zero temperature a quantum system possesses vacuum energy and there exists the possibility that it overwhelms any adjacent barrier and/or "delocalizes"; this effect is magnified for a large effective $\hbar$.

To showcase the utility of these results, we reexamine the widely studied quantum 3-spin model, presenting 3-body interactions of uniform strength between all qubit triples. It is revealed, contrary to previous thinking, that a crossover from hard to easy solution is indeed possible, with nonstoquastic drivers. (In Appendix D we further discuss the somewhat simpler Lipkin-Meshkov-Glick model [12,13] that again has long-range order but only 2-local interactions in the presence of both transverse and longitudinal fields. Such a setting may be more amenable to near-term experimental verification of coherent catalysis, given some of the latest advances in quantum computing hardware [14].) We choose to examine these highly symmetric "toy" Hamiltonians with no topological features as they are analytically tractable yet exhibit first- and second-order phase transitions typical of real-world optimization problems.

II. INTRODUCING QUANTUM TRANSPORT BY VACUUM DELOCALIZATION

It is said that "a rising tide raises all ships." Traditionally one examines the potential landscape of quantum annealing problems in isolation, seeking insight from the landscape's shifting topology as the annealing progresses. That level of analysis, however, may miss some subtleties and features that allow quantum speedups where they were previously thought not possible. In essence, the Hamiltonian has both potential and kinetic energy, and the latter may play a significant role in transport. The evolution of the ground-state components is not that of a classical hill-walker exploring the contours of the potential landscape, nor that of a quantum particle tunneling underneath the barrier; it is more akin to a ship buoyed up over it *on the sea of its own vacuum energy*, Fig. 2.

It has been discovered that in certain quantum annealing models (by an external control field or coupling) the potential landscape of complex hills and valleys may be altered in the proximity of a phase change, when the quantum state tunnels from one potential well to another through an intervening barrier. The wells on either side of the barrier begin to coalesce as the intervening barrier is suppressed, "softening" the phase change from first order to second order (or discontinuous to

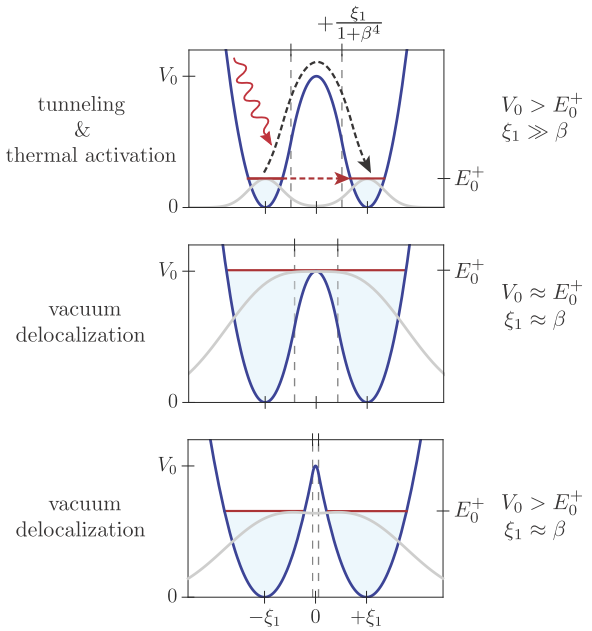

FIG. 2. Three quantum transport mechanisms exist in a double well during annealing. The potential barrier (dark blue curve) has height V_0 and the vacuum energy is E_0^+ (red horizontal line). The inverted parabola centered at the origin is stitched to two parabolic wells centered on $\pm\xi_1$ with characteristic width β. The join location is $\xi = \pm\xi_1/(1+\beta^4)$ (vertical dashed lines in all subplots). The upper panel indicates two well-understood mechanisms of quantum tunneling (red dashed line) through the barrier and classical activation over the barrier (black dashed line) following absorption by a thermal photon from the environment. The ground state is shown as a gray profile in all three panels. Tunneling and thermal activation are possible transport mechanisms when the wells are far apart, $\xi_1 \gg \beta$, and the barrier is larger than the vacuum energy, $V_0 > E_0^+$. There is, however, another transport mechanism, *vacuum delocalization*, that comes into play when the width of the ground state in one isolated well approaches the well separation, i.e., $\beta \approx \xi_1$, perhaps initiated by some external catalysis. This "Rayleigh limit" may occur when the vacuum energy subsumes the barrier, as in the middle panel. While sufficient for delocalization, this is by no means a necessary condition—as the lower panel demonstrates. The potential in this lower panel has values $(\alpha, \beta) \mapsto (2, 2)$, as compared with $\mapsto (3, 1)$ in the upper panel, and $\mapsto (1.08, 1.08)$ in the middle panel.

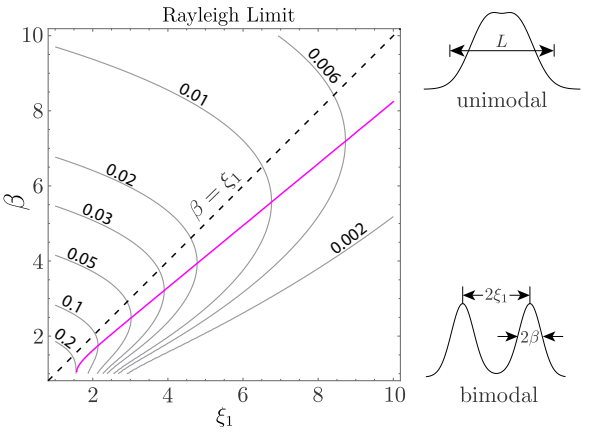

FIG. 3. Contour plot of isogaps (constant spectral gap Δ_{01}) in $\{\xi_1, \beta\}$ parameter space for the potential of Sec. III. Rayleigh limit is indicated by magenta line. As in the previous figure, the effective width of the wells vs the width of the top of the barrier is characterized by the ratio $\beta = \sigma_1/\sigma_*$ from Eqs. (A2). The distance between the well minima is $2\xi_1$ in the same scale-free units. Gap Δ_{01} is exponentially small when the ground state is split into two localized components (lower right sketch), one in each well; $\xi_1 > \beta$. If these two parameters become comparable the gap approaches $\hbar\omega_1$ as the wells effectively merge (upper right sketch). For a bulk unimodal state of effective width L the energies and gaps will scale $\propto L^{-2}$ (particle in a box). For fixed well separation ξ_1 the magenta curve traces β values associated with a maximum gap, i.e., where the indicated isogap contours are vertical. This line asymptotes to $\beta \sim 0.82\xi_1$. For larger β (above the magenta line) Δ_{01} remains large but the well energies and gaps decrease as $1/\beta^2$, no longer exponentially.

continuous). It is sometimes assumed that the barrier must be completely razed for such a qualitative change in the characteristics of the phase change to occur. It is our observation that lowering the barrier to the scale of the vacuum energy is sufficient. This allows *the vacuum state to subsume the barrier and delocalize*. In tandem, the adiabatic transfer of the quantum state between the wells proceeds at an exponentially increased rate. Interestingly, we shall see that the more fundamental condition for this enhanced mobility is that the ground-state profile be at the point of coalescing from bimodal to unimodal; see Fig. 2. This limit we refer to as the Rayleigh limit, for obvious reasons, examined further in Fig. 3. At such a point, the system may be considered as a "particle in a box," the dimension of the box corresponding to the width of the unimodal ground state at the phase transition. (In the antithetical scenario a large intervening barrier greatly exceeds the vacuum energy, permitting only exponentially slow quantum tunneling of a localized state from one side to the other.)

First, a thorough investigation of a double well will provide a more mathematical underpinning to the above remarks.

III. QUANTUM TRANSPORT IN A DOUBLE WELL

Since the performance of the adiabatic algorithm stems from the ability of the ground state to conquer potential barriers as it evolves towards the target state, let us examine this simplest of possible scenarios—that of a generic symmetric double well in one dimension, with real coordinate z, and centered on $z = 0$. Such models are used extensively with great success to explain phenomena such as diatomic molecular bonding in chemistry and microwave frequency oscillations between the vibrational modes of the ammonia molecule.

As the distance between two wells increases, the spectrum of energy levels is observed to pair up in doublets, each containing adjacent orthogonal symmetric and antisymmetric eigenstates. Doublets are separated in energy by $\sim\hbar\omega$ (the characteristic energy of one well taken in isolation) but the intradoublet splitting itself shrinks exponentially small in the well separation. See Fig. 1. By this exercise, and in the spirit of Gamow's work [4] mentioned earlier, we wish to gain insights about any crossover in the scaling behavior of these spectral gaps as the wells' distance varies. For the execution

of the adiabatic algorithm, the gap size fundamentally dictates time to solution. To foster confidence in the veracity of this statement we present the following illustration.

Supposing the system begins in the ground state of the left well, we can calculate the probability it will migrate to the right well. Assume the true ground state of the system is a real-valued positive set of amplitudes that corresponds to an equal superposition $\psi_0^+(z) = [\psi_0(z - z_1) + \psi_0(z + z_1)]/\sqrt{2}$ of the local simple harmonic oscillator ground states confined to the left and right wells. This is a reasonable assumption for wells separated by a wide barrier. Near a minimum the potential is by definition quadratic: $V(z \approx z_1) = V_0 + V_0''(z - z_1)^2$; we recall that the eigenstates of a simple harmonic oscillator are Hermite functions, with the ground state Gaussian-distributed: $\psi_0(z) \propto \exp\{-z^2/(2\sigma^2)\}$, where $\sigma = \sqrt{\hbar/(m\omega)}$ provides a natural length scale and $\omega = \sqrt{V_0''/m}$ relates the energy scale of local quanta to the well curvature. Equally, we can assume the first excited state is the antisymmetric superposition $\psi_0^-(z) = [\psi_0(z - z_1) - \psi_0(z + z_1)]/\sqrt{2}$, as its orthogonality to the ground state is guaranteed, even when the overlap $\int \psi_0(z - z_1)\psi_0(z + z_1)dz$ becomes substantial. The symmetry of the potential energy $V(z) = V(-z)$ guarantees that eigenstates will have definite even-odd parity, $\psi_k^{\pm}(z) = \pm\psi_k^{\pm}(-z)$, where k labels a particular doublet. The Sturm-Liouville theorem [15] dictates that in one dimension there can be no degeneracies, and that the odd-even doublets will be paired with the odd states above the even ones in energy [16].

Now to relate the spectral gap size to the rate of migration across the barrier for the two-state model: Taking the Hamiltonian to be quasistatic during the transition, a particle localized in the left well, at $t = 0$, will be $\psi_0(z - z_1) \propto \psi_0^+ - \psi_0^-$, which evolves to

$$\begin{aligned}\psi(z,t) &= \exp\{-iE_0^+ t/\hbar\}\psi_0^+ - \exp\{-iE_0^- t/\hbar\}\psi_0^- \\ &= \exp\left\{\frac{-i(E_0^+ + E_0^-)t}{2\hbar}\right\} \\ &\quad \times \left\{(\psi_0^+ + \psi_0^-)\cos\frac{t\Delta}{2\hbar} + i(\psi_0^+ - \psi_0^-)\sin\frac{t\Delta}{2\hbar}\right\}\end{aligned} \tag{1}$$

(ignoring normalization), and $\Delta = E_0^- - E_0^+$ is the energy gap. The system oscillates back and forth between the two wells at a frequency $\Delta/(2\hbar)$, and a characteristic timescale for the migration from left to right well is

$$\tau \sim h/\Delta. \tag{2}$$

Armed with the knowledge that barrier migration occurs on timescales varying inversely with the size of the spectral gap, one is motivated to understand how the latter varies with the height of the barrier and the distance between the two wells. This has been a heavily researched topic in the limit of tall barriers and large separations [17]; however the behavior in transition to lower barriers and small separations is not well documented.

If we demand the double well to be continuous, smooth and piecewise-parabolic, the barrier height can be calculated:

$$V_0 = \frac{mz_1^2}{2}\left(\frac{1}{\omega_*^2} + \frac{1}{\omega_1^2}\right)^{-1}. \tag{3}$$

At the barrier summit we define a characteristic frequency $\omega_* = \sqrt{-V_0''/m_*}$ and a length scale by $\sigma_* = \sqrt{\hbar/(m_*\omega_*)}$: the width of a localized ground state, were the maximum inverted. Analogously we can define $\sigma_1 = \sqrt{\hbar/(m_1\omega_1)}$, the width of a localized ground state in one of the two wells with frequency, $\omega_1 = \sqrt{V_1''/m_1}$. This "Frankensteined" potential represents a restricted subset of all possible double wells but its modest formulation, we hope, will produce insights that generalize well to the wider domain (for instance, when we examine the quantum 3-spin model in Sec. V). One might arbitrarily imagine wells with more elaborate structure away from the well extrema, without revealing much about quantum transport mechanisms in general. As was stated earlier, it is not the barrier height, or even its size relative to the ground-state energy, that establishes the spectral gap and computational complexity. The more correct question one should ask is whether the distinct well components have coalesced, i.e., whether a quantum Rayleigh "resolution limit" is reached.

Detailed examination of the piecewise potential and its analytical eigenstates is presented in Appendix A. Eigenstates $\phi^{\pm}$ are composed of parabolic cylinder functions; e.g., the ground state ϕ^+ is a superposition of such cylinder functions [18], called a Kummer function, Eq. (A6).

The following useful expression is derived in Appendix A for the spectral gap as a scale-free ratio:

$$\frac{\Delta_{01}}{\hbar\omega_*} = \frac{\phi_0^+(0)\frac{d\phi_0^-}{d\xi}(0)}{2\int_0^\infty \phi_0^+\phi_0^- d\xi}, \tag{4}$$

where the denominator is the semioverlap of the ground and excited states, and the variable $\xi = z/\sigma_*$ is the displacement variable (measured in units of σ_*, the effective width of the barrier summit). Substituting the analytical forms of the eigenstates, the gap function of Eq. (4) is maximized for well separation $\xi_1 = z_1/\sigma_* \mapsto 0$, demonstrating that the largest gap occurs when two wells merge. Introducing the scaled well width $\beta = \sigma_1/\sigma_*$, Fig. 3 indicates a maximum of the spectral gap in β near $\beta \approx 0.82\,\xi_1$. For distinct, localized wells ($\xi_1 \gg \beta$) the gap quickly vanishes to become exponentially small. For fixed ξ_1 and larger $\beta \gg \xi_1$ beyond its maximum, the gap shrinks again, but only polynomially quickly. This is because the coalesced well is now becoming wider as β increases. (Further reduction in the barrier height occurs but is now irrelevant.) The gap decays as the inverse square, $\Delta/(\hbar\omega_*) = 1/\beta^2 = \omega_1/\omega_*$, as should be expected; the wells are merging and the gap maps onto that of a single harmonic oscillator: $\hbar\omega_1$. We shall learn that the spread or confinement of the (unimodal) ground state is the harbinger of quantum mobility, rather than barrier suppression.

In terms of the original variables, fast adiabatic transport across a potential barrier does not depend directly on the potential barrier size, nor the curvature at the summit. Rather it depends on the violation of a Rayleigh separability criterion:

$$z_1 > \sigma_1 = \sqrt{\hbar}\left[\frac{1}{m_1 V''(z_1)}\right]^{1/4} \quad \text{(Rayleigh limit)}. \tag{5}$$

This criterion is entirely defined in terms of the potential curvature and coordinate extent in the vicinity of the well minima at $z = \pm z_1$. Quantum mechanics only enters via the coupling constant $\sqrt{\hbar}$; its value dictates the spread or confine-

ment of the ground state in a potential minimum. This may seem an odd remark, but it is relevant for later sections where an effective $\hbar(n)$ emerges that will depend on the number of qubits n; see Eq. (13).

It is not obvious how universal such a criterion might be, and whether it might be extrapolated to wells of different shape and symmetry. In a later section we tackle the quantum 3-spin, where we will encounter transitions between asymmetric double wells of a quantum particle with position-dependent mass.

IV. ASYMMETRIC POTENTIAL AND RESONANCE CONDITION

The asymmetric double well with a high barrier and widely separated minima ξ_1 and ξ_2 can be characterized as being far from the Rayleigh limit: $\xi_i \gg \beta_i$. Such a scenario is less interesting in the current context of vacuum delocalization, and has already been carefully examined, including the phenomenon of resonant tunneling, in Refs. [19–21].

When the wells begin to coalesce and $\beta_i \sim \xi_i$ one might ask now what are the conditions for quantum catalysis when the potential has asymmetry. To begin with, we must consider whether the system is at the point of a quantum phase transition. In the symmetric well it was guaranteed that the ground state represents a phase transition due to its inherent symmetry. But for a asymmetric double well, the ground state may be largely confined to the wider or deeper minimum.

To correctly identify the point of transition we should look to the barrier summit. A key observation is that the asymmetric piecewise parabolic potential still has a maximum of unit curvature there. Locally this inverted parabola has traveling wave solutions $\psi(\pm z)$: parabolic cylinder functions with imaginary arguments [18], moving to the left and right; see Appendix A. (Bound states of a double well must share the same eigenvalue and the traveling waves are mirror images of each other.) The overall solution in the vicinity of the barrier is a linear combination of these, $A\psi(z) + B\psi(-z)$.

Given the context of phase transition, if we associate the minimum spectral gap with the maximum ground-state variance, this maximum is only possible when the state is as equally distributed as possible between the two asymmetric wells. By matching energy levels and introducing the boundary condition at the barrier summit $\psi'(z_*) = 0$, it is as if we have introduced a double-sided mirror; each side of the barrier has a ground state that is one half of a fully symmetric double well. This is the key to an evenly distributed wave function between the two asymmetric wells. So the real-valued symmetric combination ($A = B$ above) is the only possibility.

Once this Kummer wave function (A6) is matched to the solutions farther out in each of the two wells of different widths and depths, it will be stitched to a different decaying solution as $z \mapsto \pm\infty$. The join points will differ on each side because of the asymmetry, $\xi = -\xi_1/(1+\beta_1^4)$ and $\xi = +\xi_2/(1+\beta_2^4)$. The overall ground state will look like the ground state of a symmetric double well for $z < 0$ joined at $z = 0$ to the ground state for a *different* symmetric double well for $z > 0$. It is necessary that the two symmetric wells have the same ground-state energy; all the stitched-together ground-state components must share the same eigenvalue to represent a composite eigenstate. See Fig. 4.

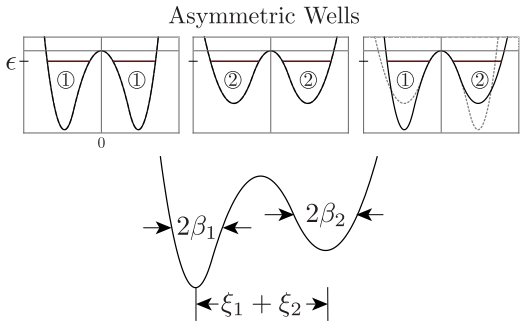

FIG. 4. An asymmetric well may also be modeled as piecewise parabolic, with two location and two width parameters, $\{\xi_{1,2}, \beta_{1,2}\}$, respectively. Here we have chosen different width parameters $\{\beta_1, \beta_2\} \mapsto \{1, 3^{-1/4}\}$ for all plots, and equal location parameters $\xi_1 = \xi_2 \approx 1.25$. These values correspond to the optimal catalysis of the quantum 3-spin; see Eq. (22). To identify the point of phase transition at the barrier summit the vacuum energy ϵ of all three potentials must coincide: the asymmetric potential and *both* symmetric wells from which it is composed (vacuum energy level depicted by red horizontal lines). Near the barrier summit the potential is an inverted parabola; the ground state has identical analytical form in all three cases (upper plots): a standing wave formed from right- and left-moving parabolic cylinder functions (see Appendix A for further discussion). Without this resonance condition we cannot assume that the ground state represents a system at the point of phase transition. Figure 19 illustrates the different phenomenon of resonance tunneling for slow phase transitions where neither well approaches the Rayleigh limit and the barrier greatly exceeds the vacuum energy.

Thus we have a *resonance* condition analogous to the one for tunneling through high barriers mentioned at the start of this section: Phase transitions in asymmetric double wells occur when the ground states of the two symmetric double wells (from which the asymmetric well is derived) have the same energy deficit below the barrier summit.

V. INTRODUCING THE FERROMAGNETIC 3-SPIN MODEL

Now let us apply this delocalization transport mechanism to systems of n spins or qubits. We can define a quantum annealing Hamiltonian as follows:

$$\hat{H} = -\Gamma\frac{\hat{J}_x}{j} - (1-\Gamma)\frac{\hat{J}_z^p}{j^p}, \tag{6}$$

where Γ is an annealing parameter. The operators $\hat{J}_{x,y,z}$ are associated with spin along the three Euclidean axes. Scalar j is a total spin quantum number, and p is an integer power. The control parameter Γ is typically initialized at 1 and reduced slowly and smoothly to 0. In the current context Γ is associated with the strength of a transverse magnetic field (along the x direction). In the usual sense, $\hat{J}_z^p$ is therefore the "target" or "problem" Hamiltonian. (The quantum annealing prepares the ground state of a problem Hamiltonian.)

As it is written, the Hamiltonian is bounded: $|\hat{H}| < 1$ This model is called quantum ferromagnetic p-spin, and we

will explore the $p = 3$ case. It is worthy of a comment that the limiting case $p \sim \infty$ faithfully represents the annealing formulation of Grover's unstructured search problem, which belongs to the class of hard problems mentioned in the introduction. Since, for example, $\hat{J}_z = \sum_i \sigma_z^{(i)}/2$ is a collective spin operator, the interaction term with $p = 3$ gives rise to 3-local interactions of type $\sigma_z^{(i)} \otimes \sigma_z^{(j)} \otimes \sigma_z^{(k)}$. This may seem at first to be somewhat unphysical. The advantage for us is that despite the uniform and infinite-range couplings and no topological features, the model exhibits a first-order phase transition for a particular Γ_c. It may provide insights about the nature of "hard" problems in quantum annealing.

By the addition of a second control parameter $\kappa \in [0, 1]$, which varies the strength of a transverse antiferromagnetic coupling $\sigma_x^{(i)} \otimes \sigma_x^{(j)}$, the 3-spin model becomes more interesting:

$$\hat{H} = -\Gamma \frac{\hat{J}_x}{j} - \kappa(1-\Gamma)\frac{\hat{J}_z^p}{j^p} + (1-\Gamma)(1-\kappa)\frac{\hat{J}_x^2}{j^2}. \quad (7)$$

It should be noted that this second control Hamiltonian $+\hat{J}_x^2$ has opposite sign to the other terms, which implies that in the computational basis the off-diagonal terms are no longer real and nonpositive. This is a definition of nonstoquasticity. It has been conjectured that the inclusion of such nonstoquastic terms might be crucial to any speedup of quantum annealing over classical computation. Indeed, nonstoquastic Hamiltonians may not be simulated efficiently by classical algorithms. Seki and Nishimori proved in Ref. [7] that for p-spin models of $p \geqslant 4$ the inclusion of the nonstoquastic term above can, during the annealing schedule, circumvent the first-order phase transition. For $p = 3$, the mean-field analysis they performed indicates that the first-order phase transition should persist, resulting in an exponential slowdown of the adiabatic evolution. We will show that actually this is not the case; even for $p = 3$ there is the possibility of nonstoquastic speedup.

The nonstoquastic term has the effect of widening the spectral gap at the phase transition. Equivalently, the free-energy landscape is altered such that potential barriers are suppressed entirely into second-order phase transitions. Traversing the fully lowered barrier, the ground state no longer jumps discontinuously at the phase transition; rather it stretches across the valley floor to occupy the other well, with amplitudes that "smear" across the intervening coordinate space (see Fig. 5).

VI. MEAN-FIELD PICTURE

In a conventional treatment one proceeds with a mean-field analysis. In such an approach, all n qubits are unentangled and identical, collectively forming a large spin-coherent state:

$$|\psi\rangle = \cos(\theta/2)|0\rangle + \sin(\theta/2)|1\rangle, \quad (8)$$

$$|\Psi\rangle = |\psi\rangle^{\otimes n}. \quad (9)$$

This state, because all the qubits are identical, is also in the $j = n/2$ fully symmetric subspace. Also note the qubit is confined to the x-z plane just like the Hamiltonian, and that θ is the polar angle made by the spin-coherent state with the x axis. If we take the expectation value of $\hat{H}$ with $|\Psi\rangle$ we can write it in terms of $\{\Gamma, \kappa, \theta\}$ parameters:

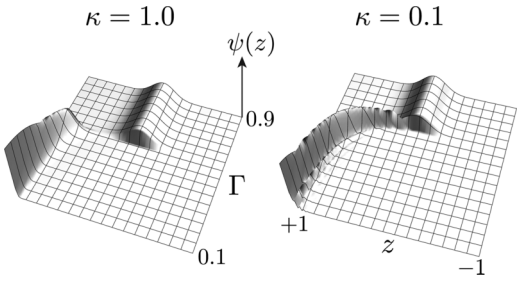

FIG. 5. In the quantum 3-spin model, increasing the antiferromagnetic coupling governed by $(1-\kappa)$ from Eq. (7) "softens" the discontinuous or first-order phase transition occurring for the external magnetic field parameter $\Gamma = 0.565$, to approach a continuous or second-order transition nearby. This is illustrated above for $n = 100$ spins. For $\kappa = 1$ the discontinuity in the ground state [amplitudes $\psi(z)$ on the vertical axis] is quite apparent as it tunnels from the paramagnetic phase centered on $z = m/j = 0$ to the ferromagnetic phase near $z = +1$. For $\kappa = 0.1$, this transition has been "smeared out" by the contribution of the nonstoquastic driver $+\hat{J}_x^2$; the state distribution changes continuously with Γ in the second plot.

$$\langle \hat{H} \rangle = -\Gamma \cos\theta - \kappa(1-\Gamma)\sin^p\theta + (1-\Gamma)(1-\kappa)\cos^2\theta. \quad (10)$$

In Cartesian coordinates, we may express $\sin\theta = z$ and $\cos\theta = x = \sqrt{1-z^2}$ and introduce the annealing ratio $\gamma = \Gamma/(1-\Gamma)$:

$$\frac{\langle \hat{H} \rangle}{\Gamma} = V(z) = -\sqrt{1-z^2} - \left[\frac{\kappa}{\gamma}\right] z^p + \left[\frac{1-\kappa}{\gamma}\right](1-z^2). \quad (11)$$

This is a mean-field description of the energy $V(z)$ as a function on the line $z = m/j \in [-1, 1]$, where m is the magnetic quantum number. We continue in the fully symmetric space of maximum spin $j = n/2$, as the Hamiltonian always commutes with the total spin operator $\vec{J}^2 = \hat{J}_x^2 + \hat{J}_y^2 + \hat{J}_z^2$ for all $\{\Gamma, \kappa\}$ values. This energy function on the line will continuously change as κ and Γ are varied, and if the changes are made adiabatically, the spin configuration remains in the minimum of this function. Equivalently, the overall spin-coherent state is like a macroscopic pointer oriented in the direction θ_0 associated with the minimum energy.

Of course, even though much can be gained from this classical analysis, this does not provide a complete picture. The spins are highly coupled with long-range order and during its evolution the system undergoes a first- or second-order phase transition. It is hard to believe that a description devoid of entanglement and other quantum properties will capture the correct characteristics in proximity to the phase transition where quantum features are dominant (e.g., peaks in entanglement and quantum Fisher information). Recall also that the bottlenecks occurring in this critical region dictate the overall time complexity of the algorithm. We now illustrate this shortcoming with the $p = 3$ case.

VII. FULL QUANTUM MODEL OF 3-SPIN WITH NONSTOQUASTIC DRIVER

First, let us make the problem *fully* quantum. We could simply proceed by numerical diagonalization of the spin Hamiltonian, but this provides little insight about the problem or its characteristic features, and does not answer questions such as, Why is there a phase transition? or Why should we expect universality to the problem's behavior for different n? Why should we expect the problem to compute quickly or slowly? And eventually, one might imagine running out of processing power to perform the numerical computations at large n. The approach we employ is to turn the discrete spin problem into a continuous variable Schrödinger equation for a particle in a potential. By similar techniques, we previously studied criticality as a resource for quantum metrology in the Lipkin model [22]. Using notation $\hat{J}_z|m\rangle = m|m\rangle$, designate the ground state as $|\Psi_0\rangle = \sum_{m=-j}^{+j} \psi_m|m\rangle$. Let us formulate the difference equation, or recurrence relations for the Hamiltonian, featuring $\psi_m, \psi_{m\pm1}$, etc., which for small $q = 2$ in $\hat{J}_x^q$ will not have many entries far from the leading diagonal. Forming the inner product $\frac{1}{\Gamma}\langle m|\hat{H}|\Psi_0\rangle$,

$$= -\frac{\kappa}{\gamma}\left(\frac{m}{j}\right)^p + \langle m|\left\{-\left(\frac{\hat{J}_x}{j}\right) + \left[\frac{1-\kappa}{\gamma}\right]\left(\frac{\hat{J}_x}{j}\right)^2\right\}|\Psi_0\rangle.$$

To proceed we recall $\hat{J}_x = (\hat{J}^+ + \hat{J}^-)/2$ and the action of these ladder operators is

$$\hat{J}^\pm|m\rangle = \sqrt{j^2 - m^2 + j \mp m}\,|m \pm 1\rangle.$$

Operating with the Hermitian spin operators to the left on the basis states $\langle m| \leftarrow$ gives

$$\langle m|\left(\frac{\hat{J}_x}{j}\right) = \frac{\sqrt{j^2-m^2}}{2j}\left[\langle m-1|\sqrt{1+\frac{1}{j-m}} + \langle m+1|\sqrt{1+\frac{1}{j+m}}\right]. \tag{12}$$

Similarly, $\hat{J}_x^q$ for $q = 2$ maps the $|m\rangle$ component into itself and $|m \pm 2\rangle$. Moving to pseudocontinuous coordinate $z = m/j \in [-1, 1]$ we introduce a small parameter,

$$\hbar = 1/j \quad \text{(effective Planck constant)}, \tag{13}$$

and rewrite $\langle m \pm 1|\Psi_0\rangle = \psi_{m\pm1} \mapsto \psi(z \pm \hbar)$. The exact result (before any approximation) is

$$\langle m|\left(\frac{\hat{J}_x}{j}\right)|\Psi_0\rangle = \sqrt{1-z^2}\left[\psi(z-\hbar)\sqrt{1+\frac{\hbar}{1-z}} + \psi(z+\hbar)\sqrt{1+\frac{\hbar}{1+z}}\right]. \tag{14}$$

The penultimate step is to identify a shift operator,

$$\psi(z \pm \hbar) = e^{\pm\hbar D}\psi(z) = \exp\left\{\pm\hbar\frac{d}{dz}\right\}\psi(z), \tag{15}$$

in terms of the differential operator $D = d/dz$, the generator of translations in one dimension.

Finally, we expand everything to second order in the small parameter $\hbar$. This is only valid when the quantum state and the form of the potential are sufficiently smooth: $\hbar^2 D^2 \ll \hbar D \ll 1$, which may not always be the case. There are errors associated with truncation to $O(\hbar^2)$, but these should be less significant for larger qubit ensembles $n = 2j \gg 1$, resulting in the effective $\hbar \ll 1$. Then combinations like $\psi(z+\hbar) + \psi(z-\hbar)$ map to $\cosh(\hbar D)\psi(z) \approx [1 + (\hbar D)^2/2]\psi(z)$. As a consequence, transverse field term $\hat{J}_z$, as well as contributing to the potential energy, is the origin of a kinetic energy term $-\frac{\hbar^2}{2}\frac{d^2\psi}{dz^2}$ in the Schrödinger equation. In some sense, the transverse field *provides* the kinetic energy that allows the quantum system to migrate through barriers.

All transverse terms of form $\hat{J}_x^q$ contribute to both kinetic and potential energy terms in the Hamiltonian:

$$\langle m|\left(\frac{\hat{J}_x}{j}\right)^q|\Psi\rangle \mapsto \left[\frac{q\hbar^2}{2}D(1-z^2)^{\frac{q}{2}}D + (1-z^2)^{\frac{q}{2}}\right]\psi(z). \tag{16}$$

Note the slightly unusual form of the kinetic energy operator for a variable mass, written in a manifestly Hermitian form: $\hat{P}\hat{M}^{-1}\hat{P}/2$ (although such a position-dependent mass does occur in the semiconductor tunneling literature [23]). Here, momentum operator $\hat{P} = -i\hbar D$ and inverse mass

$$M^{-1}(z) = -q(1-z^2)^{\frac{q}{2}}. \tag{17}$$

The potential energy contribution to $V(z)$ from the above mapping of $\hat{J}_x^q$ is $+(1-z^2)^{\frac{q}{2}}$. An analytical treatment of the Schrödinger equation with position-dependent mass was presented in Ref. [24].

Now we are at a point where we can write out the eigenequation $\hat{H}|\Psi_k\rangle = E_k|\Psi_k\rangle$ reformulated for a single particle of variable mass in a continuous potential:

$$\left[\frac{1}{2}\hat{P}\hat{M}^{-1}\hat{P} + V(z)\right]\psi_k(z) = \frac{E_k}{\Gamma}\psi_k(z). \tag{18}$$

The inverse mass operator can be zero or negative in the parameter space of $\{\Gamma, \kappa\}$:

$$\hat{M}^{-1}(z) = \sqrt{1-z^2} - 2(1-z^2)\left[\frac{1-\kappa}{\gamma}\right]. \tag{19}$$

Despite the fact this was a completely different approach to the mean-field or classical spin derivation, the potential energy $V(z)$ coincides with the free energy in the mean-field picture, Eq. (11). The key improvement is that in addition to defining a potential energy surface, we now have an analytical expression for the kinetic energy. Variable mass problems are interesting in their own right, and studying this one, with its possibility of infinite and negative mass, may reveal new behaviors within the p-spin paradigm. Or these anomalies may point to limitations of a model that is only quadratic in momentum $\hat{P}$. (Interestingly, the negative mass boundary is coincident with the second-order phase transition in the $p = 3$ case.) It is also intriguing how this model will behave for mesoscopic values of n: sufficiently large to maintain the validity of the transformation to continuous variables, but small enough that the effective $\hbar = 1/j$ is of a size that the ensemble behaves in an *extravagantly* quantum manner. This

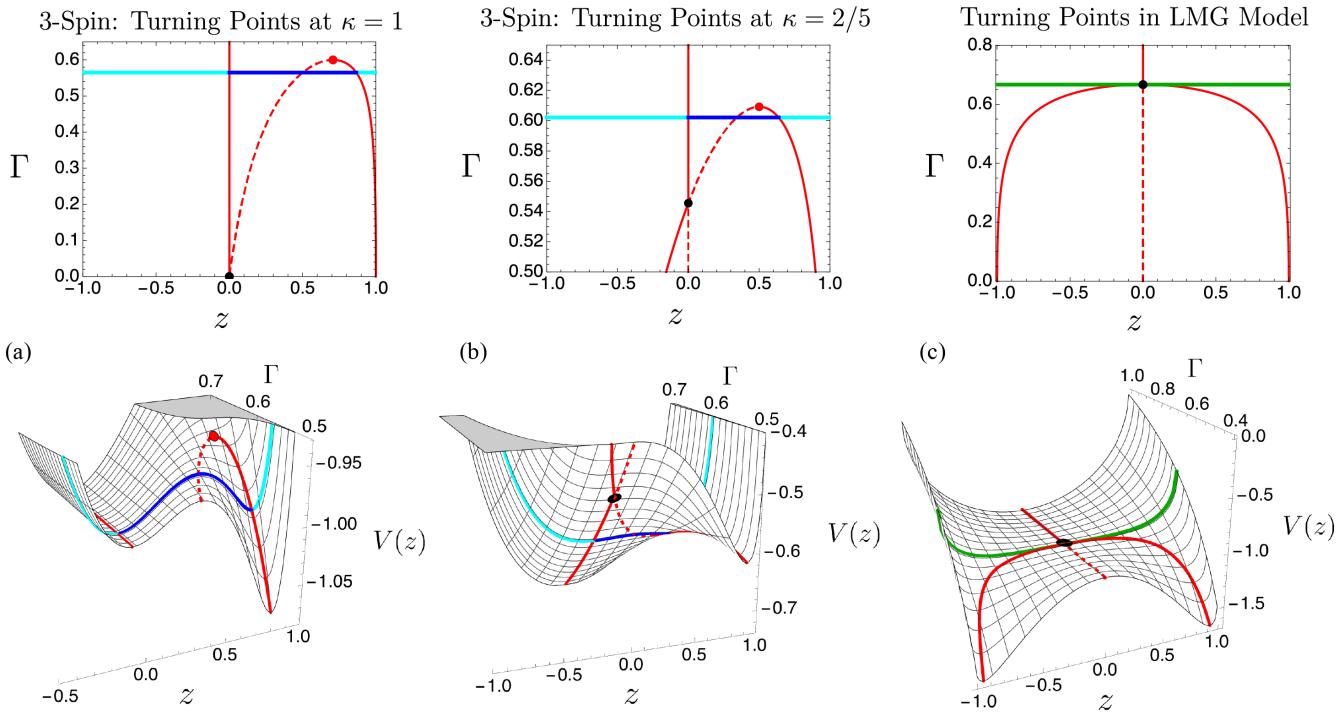

FIG. 6. Zero-temperature energy surfaces $V(z)$ associated with quantum annealing as a transverse field Γ is lowered adiabatically (upper row of 2D plots provides an overhead plan view): Coordinate $z = m/j \in [-1, 1]$ is the ratio of the magnetic quantum number m to total spin j. For an n-qubit ensemble confined to the fully symmetric subspace, the total spin $j = n/2$. Loci of the maxima (dashed red line) and minima (unbroken red line) are indicated, as are births of new maximum-minimum pairs (red dots), and second-order phase transitions where a minimum becomes a maximum (black dots). These latter points are associated with lines of zero curvature, $V''(z) = 0$. As Γ is reduced, the ground state evolves in (a) and (b) by a first-order phase transition connecting $z = 0$ via tunneling through an intervening barrier (dark blue contour) to reach the global minimum at $z = 1$. The blue and cyan contours trace out the potential wells when they have equal depth, as defines the classical first-order transition. (In the 2D plan view, the blue transition line intersects the red dashed line associated with a potential maximum, a signature of barrier penetration.) To contrast, case (c) illustrates the Lipkin-Meshkov-Glick (LMG) model [12,13], in which the ground state smoothly evolves from being localized at $z = 0$ to $z = \pm 1$, bifurcating continuously near the critical point $\Gamma_c = 2/3$ (green line). The "gentler" phase transition here is described as second order or continuous; the green contour intersects no intervening $V(z)$ maximum, and there is no barrier penetration. Cases (a) and (b) present the p-spin model for $p = 3$ which, at least classically, presents an unavoidable first-order phase transition; the barrier cannot be fully suppressed to zero. Case (b) shows the modified potential produced by the presence of the nonstoquastic catalyst term in the p-spin Hamiltonian, a transverse ferromagnetic coupling of strength $(1 - \kappa)$, as described in Sec. V. The catalysis softens the transition, bringing the first- and second-order transition points in close proximity (red and black dots of top middle figure) and effecting *partial* barrier suppression.

is the opposite extreme to the thermodynamic limit $n \sim \infty$, i.e., the classical limit $\hbar \sim 0$, where quantum effects vanish. The energy surfaces $V(z)$ for $z \in [-1, 1]$ are indicated for a range of annealing parameter Γ, two snapshots taken at values 1 and 0.4 for κ, in Figs. 6(a) and 6(b). The third subplot (c) will be discussed in Appendix D.

VIII. ADIABATIC EVOLUTION ACROSS THE SOFTENED PHASE TRANSITION

For adiabatic evolution the ground state will remain in the global minimum of the potential surface. The system begins at $\Gamma = 1$ in the unique minimum at $z = 0$; then a second minimum-maximum pair are born as the transverse field is slowly turned off. The annealing ratio at which the new minimum appears is given in Eq. (C1). The coordinate location of the new minimum is rather clumsy if expressed as $z_1(\Gamma, \kappa)$, but it can be compactly expressed as a condition in terms of the associated polar angle θ_1:

$$\sin(\theta_1) = \frac{\gamma \sec(\theta_1) + 2\kappa - 2}{3\kappa}. \tag{20}$$

This minimum $V(z_1)$ begins at a higher energy than the $z = 0$ paramagnetic minimum but sinks quickly as $\Gamma \mapsto 0$; see Fig. 6 again. During the annealing this ferromagnetic minimum drops lower than the central minimum, and it is at this point that the ground state of the system jumps discontinuously to the ferromagnetic state in a first-order phase transition. The point on the annealing schedule that corresponds to the minimum spectral gap actually occurs somewhere between the birth of the second ferromagnetic minimum and the point at which the wells have equal depth. In fact all the interesting quantum behavior of this model occurs between these extremes, outside of which a mean-field description will suffice. This is illustrated in Fig. 7, a contour plot of the $j = 40$ inverse gap $1/\Delta$ that indicates clearly a phase transition region bounded by curves associated with the birth

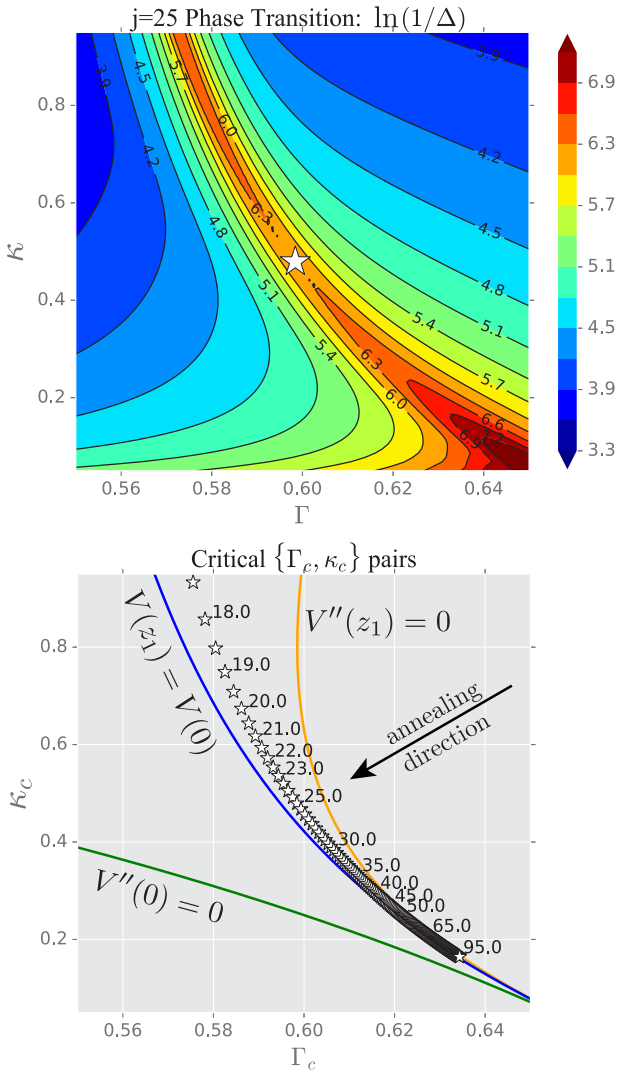

FIG. 7. Any annealing schedule that maps $\{\Gamma, \kappa\}$ values $\{1, 1\} \mapsto \{0, 1\}$ will unavoidably traverse the minimum gap region that corresponds to the phase transition of the quantum 3-spin model, Eq. (7). The phase transition ridge may not be circumvented, as is quite apparent in the upper contour plot of the inverse gap $1/\Delta$ for $n = 50$ ($j = 25$). The ridge extends throughout the full parameter range $\kappa \in [0, 1]$. Near the line $\kappa = 1$ the transition is first order; the associated minimum gap is always exponentially small in j. However, for optimized control parameters $\{\Gamma_c, \kappa_c\} = \{0.598, 0.479\}$ (denoted by a white star) the ridge defining the phase transition has a saddle, a "maximum minimum gap." Optimized annealing schedules that minimize computation time should pass near this point. In fact, for $\kappa \leqslant \kappa_c$ as $j \gg 1$ a polynomially small minimum gap is always possible, even though a classical analysis of the potential landscape alone would seemingly forbid this. The lower plot shows the $\{\Gamma_c, \kappa_c\}$ parameter pairs (stars) for different labeled $17.5 \leqslant j \leqslant 95$. (For $j \leqslant 17$, optimal $\kappa_c = 1$.) The orange and blue curves describe respectively the birth of the second potential minimum $V''(z_1) = 0$ and the point at which both wells are of equal depth, $V(z_1) = V(0)$. The green line corresponds to the second-order phase transition at $z = 0$. It is "hidden" in the sense that any adiabatic annealing schedule progressing from right ($\Gamma = 1$) to left sides will initially encounter the first-order transition from the $z = 0$ minimum to $z_1 > 0$; the green curve never crosses the blue-orange bounded region, for all κ.

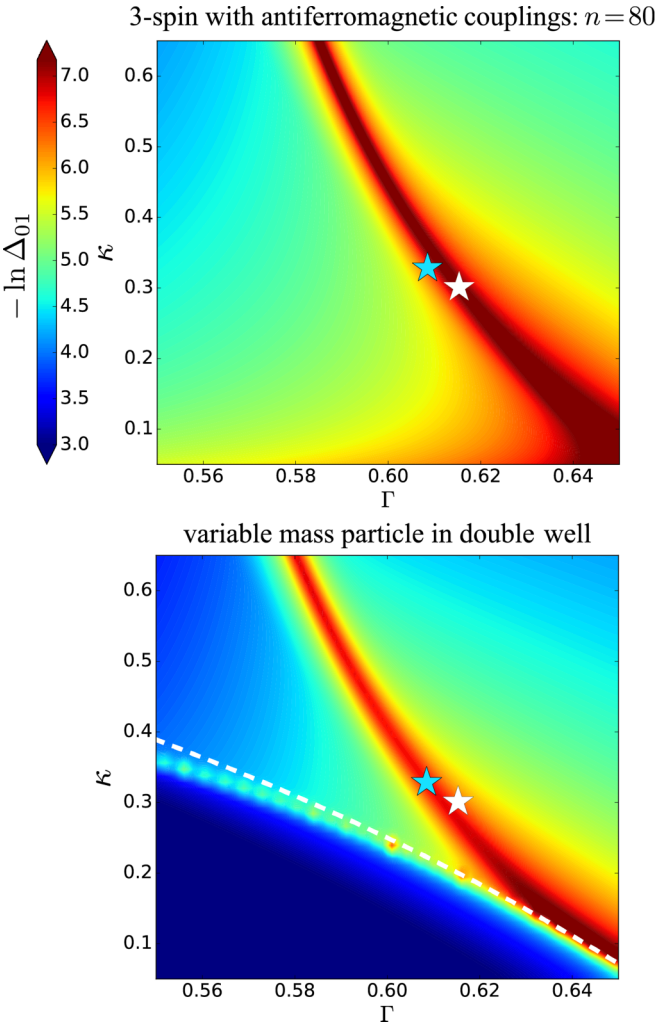

FIG. 8. For direct comparison, here are plotted the spectral gap "landscape" for both systems, as a function of the control parameters Γ (transverse field) and κ (antiferromagnetic driver). The upper plot depicts, for $n = 80$ spins, the 3-spin ensemble. The lower figure is the equivalent analytical model: a particle of variable mass moving in a one-dimensional continuous potential well. This 1D model is seen to exhibit the same qualitative features as the original spin ensemble (upper plot), except for an infinite-mass singularity at $z = 0$ coincident with the hidden second-order phase transition (white dashed curve in lower plot); see Eq. (19). The saddle point of the phase transition ridge for the original 80-spin system is indicated (in both plots) by a white star marker, and with a cyan marker for the continuous model. Ground-state wave functions associated with both models are shown in Fig. 11.

of the second minimum and the classical first-order phase transition, in orange and blue, respectively. Figure 8 compares this annealing landscape of the original n-spin ensemble and the corresponding 1D particle model we have developed, with good agreement. Finally, Fig. 18 in the Appendix B illustrates the domain of applicability of the mean-field model quite explicitly (including its failure in proximity to the phase transition).

As a side remark, we mention that in the $\{\Gamma, \kappa\}$ parameter space, for very small $\kappa \sim 0$ the gap closes very fast to be factorially or exponentially small, without any associated phase

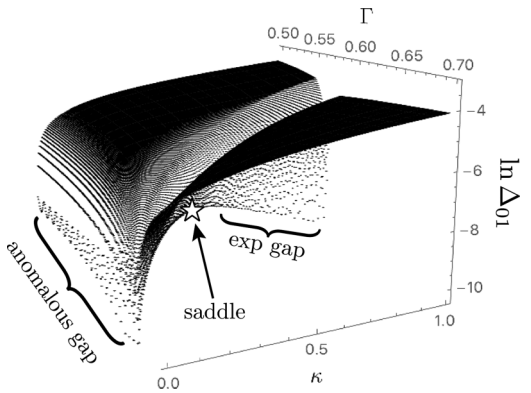

FIG. 9. The phase transition ridge features a saddle point, or "maximum minimum gap," more clearly visible in 3 dimensions when plotted against control variables κ and Γ. The energy gap of this saddle point scales polynomially with system size j. At larger κ (reducing the influence of the nonstoquastic driver) the gap size shrinks to be exponentially small in j. For very small κ the gap again quickly closes from polynomial to exponential or factorial; this anomalous gap was first discussed in Ref. [25].

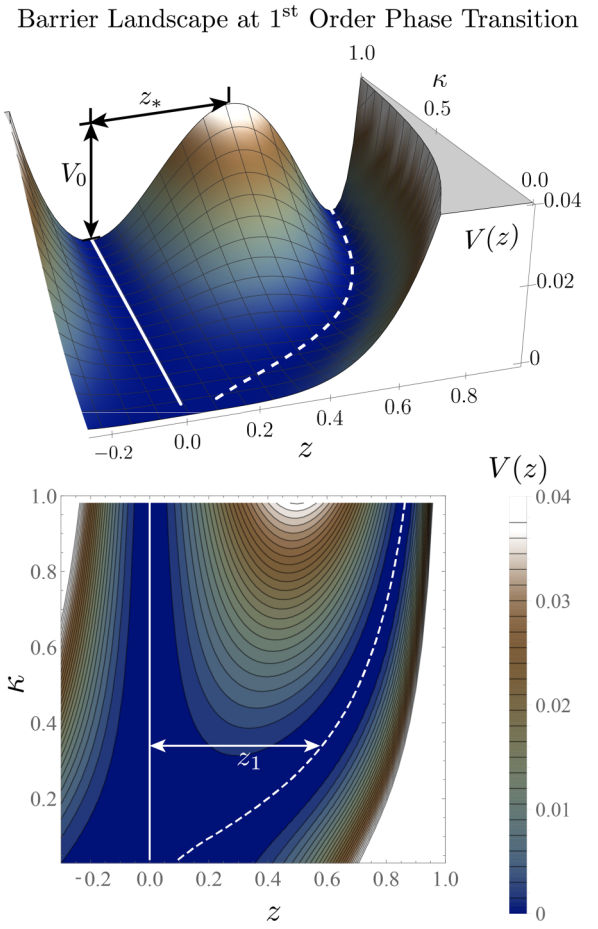

FIG. 10. For the quantum 3-spin model, the Hamiltonian contribution of the transverse antiferromagnetic driver $+(1-\kappa)\hat{J}_x^2$ is illustrated near the classical first-order phase transition (wells are of equal depth). Control parameters κ (indicated) and Γ (not shown) and are chosen to fulfill this condition, and as $\kappa \mapsto 0$ the contribution of the nonstoquastic driver increases, lowering the barrier V_0, and reducing the separation of the potential wells z_1. The paramagnetic well is centered on the origin (unbroken white line). The dashed white line describes the ferromagnetic minimum at $z = z_1$. Asymmetry of the wells is apparent even when they are of equal depth, as above.

transition; this anomalous behavior has been documented previously in Ref. [25] and relates to the fact that a finite number of spins $n = 2j$ cannot exactly represent an irrational value of the variable $z = m/j$. (In the current context this is not an interesting limit because the problem Hamiltonian vanishes when $\kappa = 0$.) See Fig. 9 for a three-dimensional visualization of the spectral gap landscape.

In Fig. 7 along the ridge of the phase transition there is a white star marker indicating the location of the saddle, or *maximum* minimum gap. As j increases we would like to know whether this optimized gap begins to shrink at a polynomial or exponential rate. In terms of classical phase transition analysis, the second-order phase transition (green arc of Fig. 7, lower plot) is always hidden behind the first-order transition (blue curve), and therefore there is no hope to produce a polynomial-sized gap. Stated using carefully chosen language in Ref. [26]: Upon examining the potential surface,"the first-order transition line persists down to $\kappa = 0$. This fact may be interpreted in terms of the Landau theory of phase transitions that there would appear a cubic term in the Landau free energy for the cubic Hamiltonian with $p = 3$, which strongly enhances the possibility of first-order transition."

Here the authors are referring to the cubic term that arises in Eq. (11), setting $p = 3$. The apparent inevitability of barrier penetration via tunneling, with the associated exponentially small spectral gaps and first-order phase transitions in many quantum annealing landscapes (beyond simple p-spin models, e.g., spin glasses), is a phenomenon much cited in arguments against the efficiency of the adiabatic algorithm for practical problems [5]. This is somewhat ironic: tunneling itself is one of the vaunted traits of quantum annealing that offer it an advantage over classical algorithms. Let us examine what happens to the double well as κ is reduced, turning on the influence of the nonstoquastic antiferromagnetic driver $+\hat{J}_x^2$.

From Fig. 10 it is seen that reducing κ also lowers the barrier; it becomes completely suppressed only for $\kappa = 0$. This limit, however, brings us back to the anomalous case discussed earlier [25]. How does the optimal nonstoquastic driver contribution κ_c scale with the system size $n = 2j$? If κ_c approaches zero too quickly it suggests that the nonstoquastic terms may not be very useful for larger ensembles. More crucially, what gap scaling can we achieve, even without being able to suppress the barrier entirely?

Algebraic analysis of the $\kappa \ll 1$ limit (Appendix C) shows at small κ (strong nonstoquastic driving) the coordinate distances z_1, characteristic frequencies ω, and barrier heights V_0 scale $\mapsto \{\kappa, \kappa^2, \kappa^4\}$, respectively. And application of Rayleigh criterion from Eq. (5) indicates a scaling law at the saddle point:

$$\kappa_c \sim O(\sqrt{\hbar}) = \alpha/\sqrt{j}, \tag{21}$$

where α we shall call the "Rayleigh coefficient."

This is encouraging, first because it vindicates our choice to work in the limit of small κ for larger ensembles. Also, it

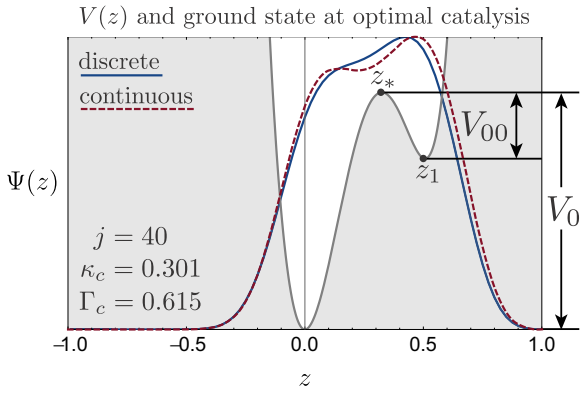

FIG. 11. The Rayleigh limit is clearly violated at optimal catalysis for both the original discrete spin system and the continuous model, i.e., for the widest minimum gap Δ_{01}, here illustrated for $n = 80$ qubits. Optimal control parameters $\{\Gamma_c, \kappa_c\}$ were found for the spin system by numerical search using a truncated Newton method. The ground state $\Psi(z)$ (blue and dashed red curves) no longer has isolated components in each well; they are largely coalesced. Note the asymmetry, not only of the potential well $V(z)$ (gray filled curve), but of the wave function, biased towards the ferromagnetic well (centered on z_1).

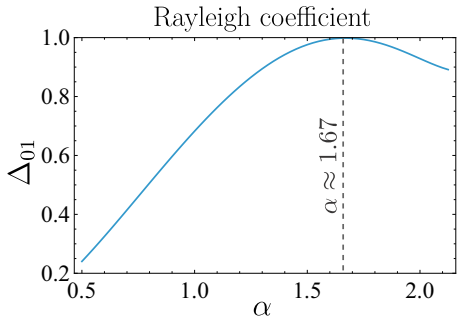

FIG. 12. The spectral gap Δ_{01} in the 3-spin is formed by multiplying the $O(1)$ gap in scale-free coordinates by $\hbar\omega_*$, which produces $\Delta_{01} \sim O(1/j^2)$. To find the numerical coefficient we may apply the delocalization resonance condition of Sec. IV to produce this curve of the gap (in arbitrary units) as a function of the Rayleigh coefficient α. It features a maximum at $\alpha \approx 1.67$, corresponding to the saddle of the phase transition.

says the relative strength κ of the problem Hamiltonian $-\hat{J}_z^3$ to the nonstoquastic driver $+\hat{J}_x^2$ must decay only polynomially in system size $n = 2j$. An optimal barrier will decay as $\kappa_c^4 \propto 1/j^2$. For any finite ensemble an optimized catalysis occurs for a nonzero barrier. Total barrier suppression, if it were even possible, would be suboptimal. (It is of course not possible in the 3-spin model.)

Combining Eq. (13) with Eq. (21) above, $\hbar = 1/j \propto \kappa_c^2$ for optimal catalysis, the vacuum energy for the isolated wells $\hbar\omega_{0,1}/2$ is of the same order as the potential barrier height $V_0 \sim \kappa_c^4$; all energy scales are equivalent.

Let us examine the Rayleigh limit $\xi_1 \sim \beta$ for the asymmetric potential, e.g., of Fig. 11. We may apply the phase transition resonance condition that was introduced in Sec. IV. Mapping the nonstoquastically driven 3-spin into the piecewise-parabolic potential produces

$$\{\xi_1, \beta_1, \xi_2, \beta_2\} \mapsto \left\{\frac{\alpha}{3^{1/4}},\ 1,\ \frac{\alpha}{3^{1/4}},\ \frac{1}{3^{1/4}}\right\}, \tag{22}$$

where α is the scaling coefficient of the Rayleigh criterion, to be recovered presently ($\kappa_c = \alpha/\sqrt{j}$). Asymptotic expressions for ξ, β terms in the small-κ limit are also worked out in Appendix C rather than interrupting the current narrative. The asymmetric potential in scale-free coordinates was depicted in Fig. 4.

From Eq. (4) the energy $\hbar\omega_*$ contributes a multiplicative factor α^2 to the gap Δ_{01}, using the small-κ result of Eq. (C9c). The saddle point of the phase transition (maximum minimum gap) occurs when the spectral gap times α^2 is a maximum:

$$\kappa_c \approx \frac{1.67}{\sqrt{j}}; \tag{23}$$

the explicit dependence of the gap on α is plotted in Fig. 12. (The numerical solution to the scale-free problem unlocks the fundamental scaling coefficient, universal to the 3-spin problem of any size $j \gg 1$.)

Going back to, and comparing, the original spin system, numerical results for $n \lesssim 400$ are presented in the upper plot of Fig. 13 which also asymptotes to $\kappa_c \sim 1.6/\sqrt{j}$, confirming the validity of the variable-mass model and the simplification to a piecewise-parabolic potential.

These results further suggest that smaller systems will more easily violate the Rayleigh separation criterion. In the thermodynamic or classical limit, $j \sim \infty$, it is impossible to approach this Rayleigh boundary. Classically, one will always have a first-order phase transition and exponentially small gap. More correct than "classical," we might designate this the "large-spin limit"; the framework we have illustrated remains quantum mechanical and tunneling is permissible, if unlikely.

Referencing Eq. (4) we know that $\Delta_c \sim O(1/j^2)$, with one power of $1/j$ coming from $\hbar$ and the other from ω_*; the latter was calculated at the critical κ_c in Eq. (C9c). The scale-free analysis that produced $\alpha \approx 1.67$ also provides the scaling here:

$$\Delta_c \sim \frac{\sqrt{3}}{2j^2}. \tag{24}$$

This compares remarkably well to the original 3-spin system, verified numerically to 400 qubits in the lower plot of Fig. 13.

The prediction of a crossover from an exponentially small gap to a polynomial one and the resulting quantum speedup, especially in models where it was assumed not possible, is a central result of this paper, as is the presentation of an optimized catalysis (energy barrier suppression) associated with a type of Rayleigh criterion and resonance for the quantum ground state of a double well. A peak in mobility is possible because of the competition between the increasing mass and increased localization (narrowing of potential well) of the state that occurs at lower κ. The former decreases energy scales and the latter increases them. The inclusion of kinetic energy and quantum uncertainty in the analysis may require redrawing of the boundaries in many phase diagrams produced for models such as p-spin that had previously been based on consideration of the classical potential surface alone.

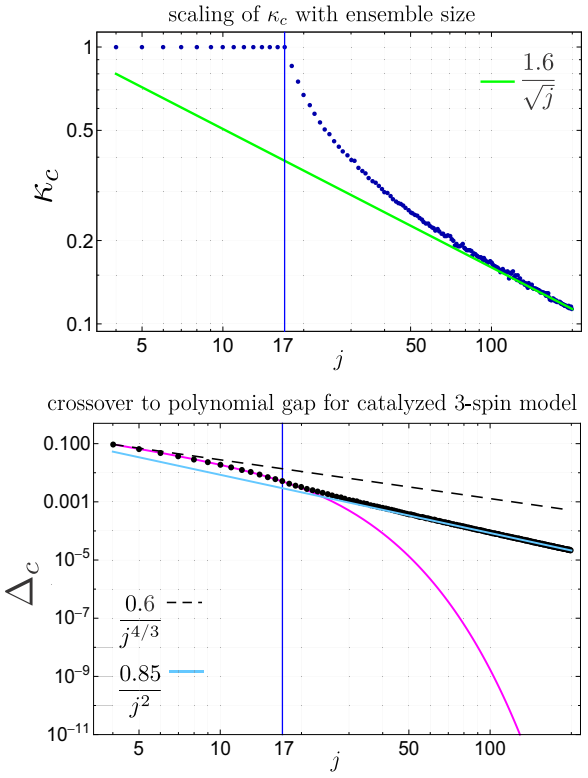

FIG. 13. Upper plot collects numerical results for the nonstoquastic control parameter κ_c of 3-spin system for $4 \leqslant j \leqslant 196$. The optimized parameter values asymptote to $\kappa_c \propto 1/\sqrt{j}$, Eq. (23). For systems of $j \leqslant 17$ apparently the ground state is always delocalized over the barrier, because the effective $\hbar = 1/j$ (and therefore vacuum energy) is large. In these cases no catalysis (no barrier suppression) is necessary to produce a polynomial gap: $\kappa_c = 1$. The lower plot shows the scaling of the minimum gap, also with system size. Even though it is forbidden from the perspective of classical phase transition theory, a polynomial gap can be maintained in the quantum 3-spin model by suppressing the potential barrier to an optimal nonzero height $V_0 \propto \kappa_c^4$. A partially lowered barrier permits the two well components to merge; at the Rayleigh limit they become a unimodal state, with polynomial spectral gap. Without any catalysis the minimum gap will quickly close at an exponential rate (magenta line), the crossover again indicated at $j \approx 17$. The exponential scaling of the uncatalyzed first-order transition asymptotes to $\Delta \sim \exp\{-0.175j\}$, as documented in Ref. [5]. The optimal gap (black dots) eventually converges on the asymptote (cyan line) predicted by the continuous model, Eq. (24). The rate of gap closure is always faster than that of the Lipkin-Meshkov-Glick (2-spin) model [12,13] $\Delta_c \propto j^{-4/3}$, a continuous phase transition. Its scaling is indicated in the lower plot by a dashed line.

IX. t^*: TIME TO SOLUTION VIA OPTIMAL PATH

Earlier we gave a simple justification in the tunneling case that time to solution and minimum gap at the phase transition are inversely related: $t^* \sim 1/\Delta_{01}(\Gamma^*, \kappa^*)$. Now we have a Hamiltonian evolving under the influence of two drivers, Γ and κ, for which we can adapt a recipe presented in Ref. [27]. With gradient operator $\nabla = (\frac{\partial}{\partial\Gamma}, \frac{\partial}{\partial\kappa})$,

$$t^* = \frac{1}{j}\int_C \frac{1}{\Delta_{01}^2}||\nabla\hat{H}||_2 \cdot (d\vec{C}). \tag{25}$$

The open curve C connects the initial point $\{\Gamma, \kappa\} = \{1, 1\}$ to the final point $\{0, 1\}$ in control space and $||M||_2$ denotes the 2-norm of a matrix M. Approximately, for the Hamiltonian of Eq. (7) in the limit $j \gg 1$ we have $||\partial\hat{H}/\partial\Gamma||_2 \sim 2 - \kappa$ and $||\partial\hat{H}/\partial\kappa||_2 \sim 1 - \Gamma$.

We believe annealing through the saddle point, identified by a star in Fig. 7, permits a fast (polynomial time) adiabatic evolution. Until now we have seen only the $1/j^2$ scaling of the gap size at the saddle; let us establish that optimal paths actually traverse the phase transition in the neighborhood of this saddle.

To investigate such paths C we can rasterize the contour landscape of Fig. 7, turning it into a grid of pixels. Each pixel becomes a node on a graph; we can use Eq. (25) to understand movement costs (time penalty) along edges connecting these nodes. Restricting movement to the $\{N, S, E, W\}$ directions (diagonal costs are not uniquely defined) means that each node or pixel is connected to at most four others. Next, we can employ a pathfinding algorithm such as that pioneered by Dijkstra in the late 1950s, Ref. [28], which uses a prioritized queue to explore the graph. The algorithm is greedy; partial paths are favored that have the lowest accumulated costs. Shortest paths found in this manner are presented in Fig. 14. We observed in Fig. 13 that the saddle moves off the straight-line path ($\kappa = 1$) connecting $\{0, 1\} \leftrightarrow \{1, 1\}$ for $j > 17$. In contrast, the pathfinding algorithm finds an optimal route that deviates from the beeline trajectory for $j \gtrsim 20$. The optimal path ventures close to the saddle point (akin to a mountain pass through the phase transition ridge) only for larger j—for instance the case $j = 40$ presented in Fig. 14.

To find an analytical answer to the scaling of this algorithm with j, we will make some approximations. First, let us assume the dominant contribution to t^* will come from the vicinity of the phase transition. In essence we want to find an effective $\delta\Gamma$, or $\delta\gamma$ corresponding to the phase transition region. We can begin by assuming the optimal path segment $\delta\vec{C}$ will traverse the transition in a direction normal to the curve γ_0 from Eq. (C1) that defines the boundary of the quantum region. In the parameter space of (κ, γ) the vector $\vec{\gamma}_0 = (\kappa, 2(1-\kappa) + 9\kappa^2/4)$ has a normal vector $\vec{n} \approx (9\kappa/2 - 2, -1)$. This produces

$$t^* \sim \frac{\delta\kappa}{j\Delta_c^2}\{O(1)\}, \tag{26}$$

where we can easily find the effective width of the phase transition $\delta\kappa$ from the intersection of the normal line with curves γ_* and γ_0; see Fig. 15.

The hidden second-order phase transition (occurring when the paramagnetic minimum at the origin $z = 0$ becomes a maximum) occurs precisely at $\gamma_2 = 2(1-\kappa)$, which is the same as γ_0 to first order in κ. The quantum phase transition must occur between γ_0 and γ_2, and therefore $t^* \sim O(\kappa^2)$ or smaller.

Numerical results of Fig. 15 suggest that $\delta\gamma \sim O(\kappa^{2.75})$ at the critical κ_c. The associated small change $\delta\kappa$ normal to the phase transition ridge must also be

$$\delta\kappa_c \sim O(\kappa^{2.75}), \tag{27}$$

when $\kappa \ll 1$. Putting all our scaling relationships together, including the Rayleigh limit $\kappa_c \sim O(j^{-1/2})$ and gap size scaling

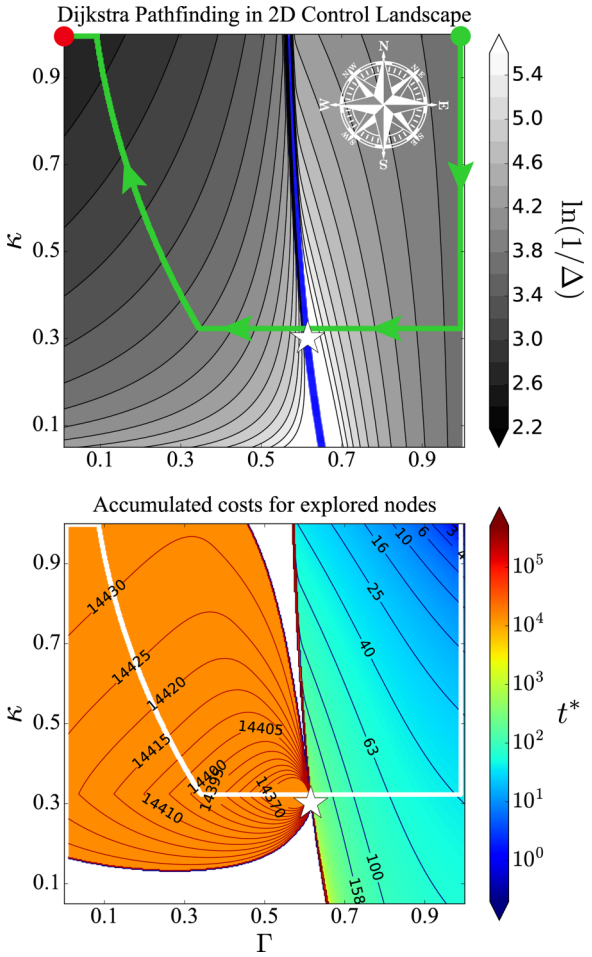

FIG. 14. The algorithm due to Dijkstra is employed on a graph produced by rasterizing the control landscape of Fig. 7, here the ensemble size $j = 40$. Contours here are also of $\log 1/\Delta_{01}$, the cost of moving between adjacent nodes $\propto 1/\Delta_{01}^2$. Darker-shaded regions may therefore be more rapidly traversed. Movement costs along graph edges, between pixels, are defined by Eq. (25). The green line represents an optimal adiabatic contour $C^*(\Gamma, \kappa)$ from the initialization parameters $\{\Gamma, \kappa\} = \{1, 1\}$ (green dot) to the final values $\{0, 1\}$ (red dot). The blue pixels of the upper plot represent the phase transition ridge, with the saddle indicated by a white star marker. One might imagine an explorer journeying south from his home in the northeast corner to cross a river close to the shallowest point before heading to his destination in the northwest. There are different anisotropic frictional movement costs for going south $(1 - \Gamma)(\delta\kappa)$ versus west, $(2 - \kappa)(\delta\Gamma)$, independently of the node cost. This explains the zero friction path traversed due south from $\{1, 1\}$ to $\sim\{1, 0.3\}$ that then turns westward towards the saddle marker. On the lower plot is t^*, the cumulative contribution to the total adiabatic time. Unexplored regions are left uncolored in the lower plot. Admittedly, there will be error in the sampling of the phase transition terrain (the ridge is basically a delta function) which might be improved by adaptive sampling of regions with steep gradients.

$\Delta_c \sim O(j^{-2})$, gives

$$t^* \sim O(j^\alpha) \tag{28}$$

for the catalyzed time complexity where we have given the analytical bound $\alpha < 2$ and numerical evidence for $n \in [1, 400]$ qubits indicates an $\alpha \sim 13/8$.

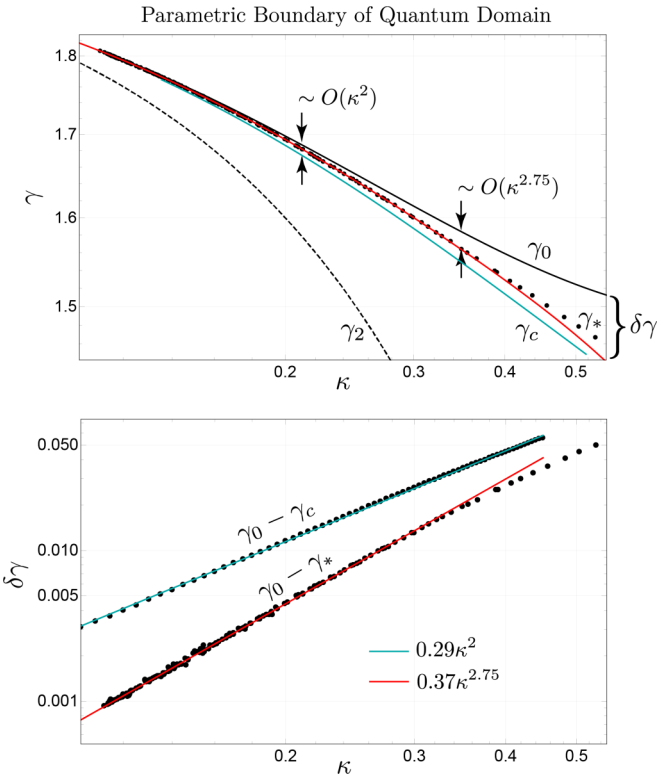

FIG. 15. In $\{\kappa, \gamma\}$ parameter space, the quantum domain exists between the birth of the ferromagnetic well in the potential at γ_0 and the point of the *classical* first-order phase transition γ_c, where the potential wells have equal depth. Also shown is the hidden second-order transition $\gamma_2 = 2(1 - \kappa)$, where the paramagnetic minimum becomes a maximum (dashed line). Between γ_c and γ_0 appears the true quantum phase transition at γ_*. Scaling of $\gamma_0 - \gamma_*$ is observed between κ^2 and κ^3; a fit line for $\kappa^{2.75}$ is indicated on a logarithmic scale in the lower plot (red line).

The overall algorithmic complexity of the catalyzed 3-spin is polynomial, between linear and quadratic in the number of spins or qubits.

The continuous model's validity relies on a degree of smoothness in, e.g., the wave function and its derivative. We may be precluded from any refinement on smaller scales than $\hbar = 1/j$, e.g., in the coordinate z. Optimal catalysis has $\kappa_c \sim 1/\sqrt{j}$ so sharp effects such as locating the phase transition ridge might be associated with higher powers than κ^2, and thus may not be captured here. For these reasons we may be restricted to the statement that in parameter space, the phase transition ridge has width $1/j$ *or smaller* at the saddle point of optimal catalysis.

X. CONCLUSIONS AND OUTLOOK

One might expect that quantum mobility in a potential with tall barriers increases monotonically as those barriers are suppressed, by application of external control fields or couplings. This can result in an exponential speedup in time to solution. Some coupled-spin systems, however, exhibit a sweet spot, an optimal catalysis, where mobility depends on more than just complete barrier suppression. Indeed, that full suppression may not even be possible, and the exponential

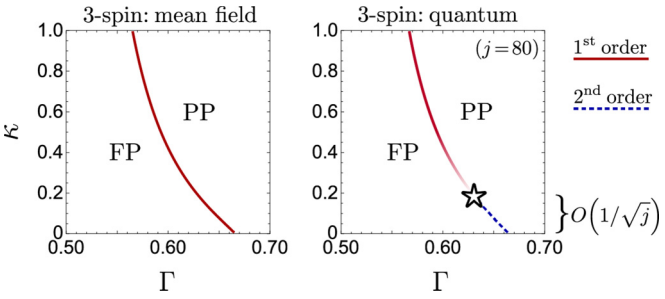

FIG. 16. A light at the end of the tunnel: Subject to a full quantum analysis, the phase portrait for the antiferromagnetically driven 3-spin must be redrawn. The boundary between paramagnetic phase (PP) and ferromagnetic phase (FP) in the space of control parameters Γ and κ is no longer first order, and admits a softer transition. This "polynomial back door" of order $1/\sqrt{j}$ bounded by the saddle point (star marker) circumvents the exponential slowdown in time-to-solution associated with tunneling; the annealing proceeds in polynomial time.

speedup seems out of reach. For instance, the 3-spin model with a nonstoquastic driver has a strong dependence on the variable mass that results in a saddle point of the barrier in parameter space.

We have shown that kinetic energy scales should not be ignored, as they are in mean-field models. The scale is set by the effective Planck constant $\hbar = 1/j$, the reciprocal ensemble size. This "quantum uncertainty" dictates the ability of a ground state to delocalize across barriers. We repurpose the Rayleigh optical separation criterion for quantum computing, and identify its violation as a harbinger of *exponentially* enhanced mobility; see Fig. 16. Also, when a double-well potential exhibits asymmetry we identify a resonance condition, allowing the quantum phase transition point to be precisely located, as distinct from the nearby classical one. The full quantum treatment of annealing through shallow barriers can lead to radically different conclusions about time complexity of the algorithm.

To illustrate this "optimized catalysis" we created an analytical model, and verified numerically via a pathfinding algorithm previously unexpected polynomial scaling (and universal coupling coefficients) of the time to solution for the quantum 3-spin catalyzed by an antiferromagnetic coupling.

In terms of future work, if typical barrier heights are known in an annealing problem, e.g., $V_0 \sim n^{1/3}$ for some spin glasses, one might match vacuum energies to that scale in our models, to effect polynomial time solutions of otherwise "hard" problems. The challenge then will be the optimal control of the Hamiltonian landscape, without leveraging prior knowledge of minimum gap and saddle or barrier locations and magnitudes. Because the vacuum delocalization effect we describe relies on mesoscopic-scale systems (a large effective $\hbar = 1/j$ balanced against larger problem instances $n = 2j$), there is motivation to distribute large computations in an optimal way among smaller quantum subsystems of, e.g., 10 to 1000 qubits.

These results hold in the adiabatic limit at zero temperature. For the nonzero-temperature case, we should assume that $kT \ll V_0$, because if $kT \sim V_0$, simulated annealing is known to be an efficient approach.

ACKNOWLEDGMENTS

I would like to express my gratitude to Waleed Kadous at Uber, Zhang Jiang at Google, Itay Hen of the University of Southern California, Birgitta Whaley, William Huggins, and Norm Tubman, all at University of California, Berkeley, and finally, Sergey Knysh, my longtime collaborator at the NASA Ames Quantum Laboratory. My thanks to each for their encouragement, diverse perspectives, and stimulating discussions as this work progressed.

APPENDIX A: DETAILS OF THE PIECEWISE-PARABOLIC POTENTIAL

In order to understand vacuum delocalization we may write a Schrödinger equation for states in the vicinity of the barrier maximum, where we will assume the potential is dominantly quadratic:

$$-\frac{\hbar^2}{2m}\frac{d^2\psi_0^+}{dz^2} + \left[V_0 - E_0^+ - \frac{m\omega_*^2}{2}z^2\right]\psi_0^+ = 0. \tag{A1}$$

It is possible that in this regime a typical WKB approach will fail; although the WKB series is an exact asymptotic expansion, its truncation to leading terms may not be justified here. (It should be noted that a successful WKB analysis on the phenomenon of quantum transport across a fully suppressed barrier was presented in Ref. [6].)

General characteristics become clearer by switching to nondimensionalized energy and length scales:

$$\xi = z/\sigma_*, \tag{A2a}$$
$$\delta^\pm = (V_0 - E^\pm)/(\hbar\omega_*), \tag{A2b}$$
$$\epsilon = V_0/(\hbar\omega_*) - \delta^+, \tag{A2c}$$
$$\beta = \sigma_1/\sigma_*, \tag{A2d}$$
$$\xi_1 = z_1/\sigma_*. \tag{A2e}$$

The rescaled energies $\delta^\pm$ are the energy deficit under the barrier summit for the ground and excited states, respectively, and measured in "quanta" $\hbar\omega_*$ of the inverted maximum [29]. The rescaled ϵ is the ground-state energy measured from the well bottom at $V = 0$. The barrier height will increase with the square of well separation ξ_1:

$$V_0 = \frac{\hbar\omega_*}{2}\left(\frac{1}{1+\beta^4}\right)\xi_1^2 = \frac{\hbar\omega_1}{2}\left(\frac{\beta^2}{1+\beta^4}\right)\xi_1^2. \tag{A3}$$

For fixed well separation ξ_1 the barrier is lowered monotonically for increasing $\beta = \sigma_1/\sigma_*$; i.e., widening the wells also suppresses the barrier. We may rewrite the Schrödinger equation for the ground and first excited states in the vicinity of the barrier maximum (that is ξ and $|\delta^\pm| \lesssim 1$) as

$$-\frac{d^2\phi_0^\pm}{d\xi^2} + (2\delta^\pm - \xi^2)\phi_0^\pm = 0, \tag{A4}$$

enabling us to "roll up" parameters such as $m, \hbar, \omega$ into the new variable ξ.

These can be solved via parabolic cylinder functions, remembering the boundary conditions that ϕ^- and $d\phi^+/d\xi$ are necessarily zero at the origin $\xi = 0$ (because ϕ^+ is an even

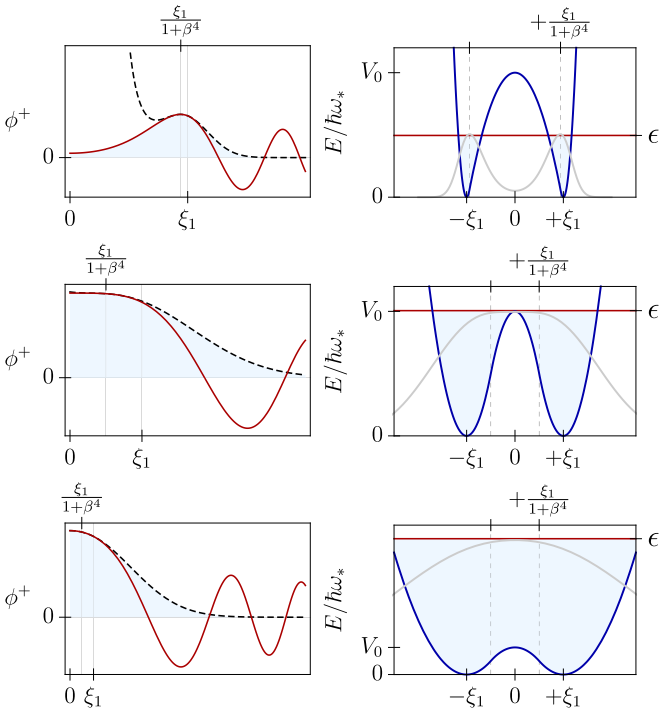

FIG. 17. In the left column the ground state ϕ^+ valid at the summit $\xi = 0$, a Kummer function from Eq. (A6) (red curve), is joined to the parabolic cylinder function of Eq. (A8) (black dashed curve) valid within the well. The area under the correct piecewise solution for ϕ^+ is shaded blue. The barrier height V_0 is proportional to the harmonic mean of the squared frequencies, Eq. (3). The particular parabolic cylinder function is chosen that decays to zero at $\xi \sim \infty$. Three cases are considered in turn, vacuum energies E^+ below, equal to, and above the barrier of height V_0, indicated in the right column, with rows corresponding to $\{\xi_1, \beta\} \mapsto \{2.5, 0.5\}, \{1.07, 1\}, \{0.5, 1\}$ values. Recall that $\pm\xi_1$ is the location of each well minimum, the ratio of well width to barrier width is $\beta = \sigma_1/\sigma_* = \sqrt{\omega_*/\omega_1} = [V''(\xi = 0)/V''(\xi = \xi_1)]^{1/4}$, and $\pm\xi_1/(1+\beta^4)$ are the "seams."

function and ϕ^- is odd). The unnormalized ground-state and excited-state solutions at the barrier summit are [18,29]

$$\phi_0^\pm = D_{-1/2+i\delta^\pm}[(1-i)\xi] \pm D_{-1/2+i\delta^\pm}[-(1-i)\xi], \quad \text{(A5)}$$

decomposed as an even and odd superposition of parabolic cylinder functions $D_\nu(az) \pm D_\nu(-az)$, respectively, with complex a, ν. The ground state is expressible as a Kummer confluent hypergeometric function, ${}_1F_1$,

$$\phi_0^+ = e^{-\frac{i\xi^2}{2}}\, {}_1F_1\left(\frac{1}{4}(1-2i\delta^+); \frac{1}{2}; i\xi^2\right), \quad \text{(A6)}$$

a real function of the scaled coordinate ξ and eigenvalue δ^+ that we have pinned to $\phi_0^+(0) = 1$ (see Fig. 17).

Moving on to the wave functions at the well minima (and beyond to $\xi \sim \pm\infty$), in the scale-free setting these are parabolic cylinder functions [30]. Examining first the well centered on $\xi = \xi_1$, the Schrödinger equation for the ground state takes a form associated with Weber:

$$-\frac{d^2\phi_0^+}{d\xi^2} + \left[\frac{(\xi-\xi_1)^2}{\beta^4} - 2\epsilon\right]\phi_0^+ = 0. \quad \text{(A7)}$$

The vacuum energy is $\epsilon = (\nu + 1/2)/\beta^2$ and for an isolated well the modified eigenvalues ν are all non-negative integers. In the case of the ground state $\nu = 0$, the associated eigenfunction would be a simple Gaussian profile, the lowest-order Hermite function, as one would expect of a simple harmonic oscillator. For a double well with very large separation $\xi_1 \gg \beta$ the ground and first excited states are well approximated by an even or odd superposition of two Gaussian components centered on each well. This becomes invalid as the wells are allowed to approach one another. (The double-Gaussian ansatz is the wrong choice of orthonormal basis to span the two-dimensional subspace of $\phi_0^\pm$.) For finite-width barriers, tunneling causes the eigenvalues to shift away from integer values and the ground state in proximity to the wells becomes again a parabolic cylinder function D_ν, this time with real noninteger ν:

$$\phi_0^\pm\left(\xi > \frac{+\xi_1}{1+\beta^4}\right) = D_{\beta^2\epsilon-\frac{1}{2}}\left[\frac{\sqrt{2}(\xi-\xi_1)}{\beta}\right]. \quad \text{(A8)}$$

Of the possible solutions to the Weber equation this particular form uniquely approaches zero in the limit $\xi \sim \infty$, a necessary boundary condition for normalization, to make the wave-function square integrable. For the left well we choose the solution that approaches zero as $\xi \sim -\infty$, actually the prior solution reflected in the y axis:

$$\phi_0^\pm\left(\xi < \frac{-\xi_1}{1+\beta^4}\right) = \pm D_{\beta^2\epsilon-\frac{1}{2}}\left[\frac{-\sqrt{2}(\xi+\xi_1)}{\beta}\right]. \quad \text{(A9)}$$

This is a guaranteed independent solution to Weber's equation, as long as $\beta^2\epsilon - \frac{1}{2}$ is not a non-negative integer. For the double well that we have constructed, the parabolic regions were stitched to the inverted parabola at $\xi = \pm\xi_1/(1+\beta^4)$ in the scale-free coordinates. We must therefore join our two ground (or excited) state solutions also at these locations. The two states above are solutions for different regions of the potential; they do not exist in superposition, unlike Eq. (A5) near the summit, where a superposition of parabolic cylinder functions was necessary to achieve the required even-odd parity about $\xi = 0$. [Note the sign change in Eq. (A9) for the excited state so it can be joined on to the odd-parity solution of Eq. (A5).]

Confining attention to $\xi > 0$ there are two conditions that allow our solutions to be matched, associated with the continuity of both the wave function and its derivative at the join. Matching Eq. (A5) to the parabolic cylinder function Eq. (A9) provides the relative amplitude of the symmetric state scattered off the potential summit. Then also matching gradients at the join is only possible for a discrete set of energy eigenvalues, the lowest of which is the vacuum energy ϵ.

We are most interested in the gap $\delta^- \leftrightarrow \delta^+$ so let us multiply Eqs. (A4) respectively by ϕ_0^- and ϕ_0^+, and then subtracting one from the other, producing

$$\frac{d^2\phi_0^-}{d\xi^2}\phi_0^+ - \frac{d^2\phi_0^+}{d\xi^2}\phi_0^- + 2\phi_0^+\phi_0^-(\delta^+ - \delta^-) = 0. \quad \text{(A10)}$$

Next we may integrate by parts, using the result

$$\int_A^B (\psi_1\psi_2'' - \psi_2\psi_1'')d\xi = (\psi_1\psi_2' - \psi_2\psi_1')\,|_A^B. \quad \text{(A11)}$$

With integration limits $\xi \in [0, \infty]$, and recalling that $\phi^-(0) = 0$ and that for normalization purposes we expect $\phi^\pm(\infty) = 0$, we arrive at

$$\frac{\Delta}{\hbar\omega_*} = |\delta^- - \delta^+| = \frac{\phi_0^+(0)\frac{d\phi_0^-}{d\xi}(0)}{2\int_0^\infty \phi_0^+\phi_0^- d\xi}, \tag{A12}$$

where the denominator is the semioverlap of the ground and excited states.

APPENDIX B: ANALYSIS OF THE PHASE TRANSITION IN THE CATALYZED 3-SPIN MODEL

Often, phase transitions in quantum spin systems are modeled using a mean-field model, where the ground state is represented as a product state of n spins (a spin-coherent state) that tracks the potential minimum during the annealing process. The validity of such a description can be investigated, both in the neighborhood of the phase transition, and far from it. Without the possibility of entanglement the model of a large rotating classical pointer falls short, in particular in the transition region, as evidenced by Fig. 18. Classically, one usually defines the phase transition as occurring when the two well minima are of equal depth, but in the quantum case we should instead nominate the minimum gap location on the annealing landscape, which itself depends on the number of spins n. Additional complications in the 3-spin model are mass that varies as a function of the well location, and the fact the double well is asymmetric at the minimum gap (see Fig. 19).

APPENDIX C: CATALYZED 3-SPIN MODEL IN THE $\kappa \ll 1$ LIMIT

In the regime $0 < \kappa \ll 1$ near the phase transition, the annealing ratio at the quantum boundary (birth of the second minimum) is

$$\gamma_0 = \frac{\sqrt{169\kappa^4 - 172\kappa^3 + 78\kappa^2 + 8\kappa - 2(\kappa-1)[\kappa(19\kappa-2)+1]^{3/2} - 2}}{6\kappa}. \tag{C1}$$

The asymptotic expansion to second order of this expression is:

$$\gamma_0 = 2(1-\kappa) + \tfrac{9}{4}\kappa^2 + O(\kappa^3). \tag{C2}$$

Interestingly, this is not a convergent series for all $\kappa \in [0, 1]$; cubic and higher terms are ignored at our peril. The hidden second-order phase transition (occurring when the paramagnetic minimum at the origin $z = 0$ becomes a maximum) occurs precisely at $\gamma_2 = 2(1-\kappa)$, which is the same as γ_0 to first order in κ. The quantum phase transition must occur between γ_0 and γ_2, and therefore must be $O(\kappa^2)$ or smaller.

We choose to parametrize this sweet spot as

$$\gamma_0 - \gamma_* = \delta\gamma = \left[\frac{x\kappa}{2}\right]^2, \tag{C3}$$

where $x \lesssim 1.07$ is a small parameter. (Value $x = 1.07$ corresponds to the classical phase transition, at which the wells have equal depth.)

The well separation within this quantum regime is

$$z_1 = \frac{(3+x)\kappa}{2} + O(\kappa^2), \tag{C4}$$

and the distance to the maximum from the minimum at the origin is

$$z_* = \frac{(3-x)\kappa}{2} + O(\kappa^2). \tag{C5}$$

The barrier summit and ferromagnetic ground state are therefore separated by

$$z_1 - z_* = \kappa x + O(\kappa^2), \tag{C6}$$

zero at $\gamma = \gamma_0$ or $x = 0$, where these two extrema merge.

The barrier, or potential difference to the summit from the minimum at $z = 0$, is polynomially dependent on κ:

$$V_0 = \frac{\kappa^4}{128}(3-x)^3(1+x) + O(\kappa^5). \tag{C7}$$

On the other side of the summit, the second minimum is below the maximum by an energy

$$V_{00} = \frac{x^3\kappa^4}{8} + O(\kappa^5). \tag{C8}$$

In the same limit, the characteristic frequencies associated with the quadratic extrema of $V(z)$ are

$$\omega_0 \approx \frac{9-x^2}{8}\kappa^2 + O(\kappa^3), \tag{C9a}$$

$$\omega_1 \approx \frac{\sqrt{3x}}{4}(3+x)\,\kappa^2 + O(\kappa^3), \tag{C9b}$$

$$\omega_* \approx \frac{\sqrt{3x}}{4}(3-x)\,\kappa^2 + O(\kappa^3). \tag{C9c}$$

To summarize, in the small-κ limit, coordinate distances, characteristic frequencies, and potential barriers scale with the nonstoquastic driver as $\mapsto \{\kappa, \kappa^2, \kappa^4\}$. Figure 10 shows at the classical phase transition point how the barrier size and shape change with κ. (The implicit Γ values are chosen to maintain the wells at equal depth as κ is varied.) At this point we underscore some of the subtleties of this 3-spin model, namely the asymmetry of the double well compounded by a position-dependent mass variable, Eq. (17). The WKB method has been discussed in the literature for tunneling under a barrier between asymmetric wells [19,21] though we find no previous work that discusses the coherent catalysis limit of a "low barrier," $\hbar\omega/2 \sim V_0$ (where lowest-order WKB truncation will likely fail). We simplify the position-dependent mass challenge by taking delta samples of the mass at the potential minima. This is a reasonable assumption for narrow wells and $j \gg 1$, but less accurate as wells become more shallow and merge. Even so, the characteristic frequency at a quadratic minimum will be $\omega(z) = \sqrt{V''(z)/m(z)}$ and the quantum ground state is "heavier" within the ferromagnetic phase centered on $z_1 > 0$ than at the $z = 0$ (paramagnetic

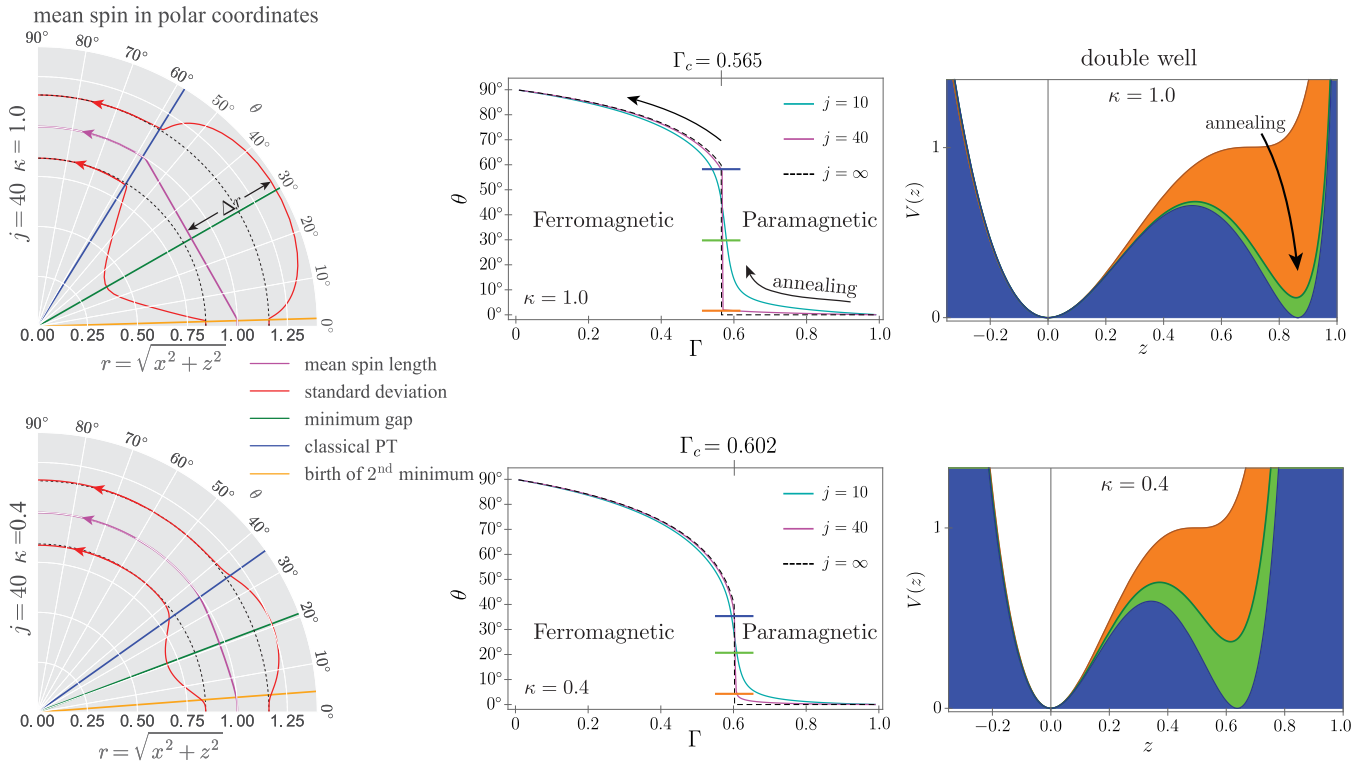

FIG. 18. Mean spin for the 3-spin model has components $\langle \vec{J} \rangle = \langle \Psi | \{ \hat{J}_x, \hat{J}_y, \hat{J}_z \} | \Psi \rangle$, normalized by the principal quantum number j. In polar coordinates the magnitude $r = |\langle \vec{J} \rangle| / j$ and angle $\theta = \arctan\{\langle \hat{J}_z \rangle / \langle \hat{J}_x \rangle\}$. The uncertainty is the standard deviation (red curves) calculated from the quantum variance, $j\Delta r = \sqrt{\Delta^2 \hat{J}_x + \Delta^2 \hat{J}_y + \Delta^2 \hat{J}_z}$. Dashed quarter circles in the polar plots correspond to uncertainty of a classical spin (a spin coherent state), constant at $1/\sqrt{j}$, in these units. Most of the quantum behavior is confined to a small parameter region $\Delta\Gamma$ close to the classical first-order phase transition (PT) value, Γ_c. Outside the region bounded by orange and blue lines the system behaves as a large rotating spin with $r = 1$, and $\Delta r = 1/\sqrt{j}$. Within this "quantum" boundary, however, the vector is quite nonclassical: $r < 1$ and $\Delta r > 1/\sqrt{j}$. The orange and blue boundary lines in the polar plot correspond to the birth of the second potential minimum and the classical phase transition, respectively. At $j = 40$ the appearance of the minimum spectral gap (green line) occurs at an angle almost exactly bisecting the quantum sector. The associated angle coincides with maximum uncertainty, Δr. Within the boundary the spin vector describes almost a straight line chord (magenta) perpendicular to the minimum gap "event" angle (green line). The phase transition is seen to be "softer" at lower spin number, e.g., $j = 10$ (cyan curves of middle column). The $j = \infty$ line (black dashed curves of middle column) tracks the global minimum of $V(z)$ exactly; this is the thermodynamic limit where the vacuum (kinetic) energy vanishes. The rightmost plots illustrates the shape of the double well for $\kappa \mapsto \{1.0, 0.4\}$ at the birth of the second minimum (orange) and at the classical phase transition (blue) and for the minimum spectral gap in the case $j = 40$ (green). Observe that at the minimum gap the potential is *not* symmetric, nor the wells of equal depth.

phase) ground state. Recall that β is a ratio of frequencies, and not a function of $\hbar$:

$$\beta = \frac{\sigma_1}{\sigma_*} \approx \sqrt{\frac{m_* \omega_*}{m_1 \omega_1}}. \tag{C10}$$

On the other hand, $\xi_1 = \Delta z / \sigma_* = \Delta z \sqrt{m_* \omega_* / \hbar}$. This is where the energy scale will enter, in terms of parameter $\hbar = 1/j$.

We shall also need the $\kappa \sim 0$ asymptotic expression for the variable masses:

$$\frac{1}{m_0} = \omega_0 \approx \frac{9 - x^2}{8} \kappa^2 + O(\kappa^3), \tag{C11a}$$

$$\frac{1}{m_1} \approx \frac{3}{4}(3 + x)\kappa^2 + O(\kappa^3), \tag{C11b}$$

$$\frac{1}{m_*} \approx \frac{3}{4}(3 - x)\kappa^2 + O(\kappa^3). \tag{C11c}$$

Notice that $m_0 \omega_0 = 1$, and therefore $\sigma_0 = 1/\sqrt{j}$. For the Rayleigh limit, powers of κ balance on both sides of $z_* \approx \sqrt{\hbar/(m_0 \omega_0)}$ only if $\hbar = O(\kappa^2)$, since $z_* = O(\kappa)$, Eq. (C5). Reordering the terms, demanding $\xi_1 \sim \beta$ leads to a scaling law at the maximum minimum spectral gap (saddle):

$$\kappa_c \sim O(1/\sqrt{j}). \tag{C12}$$

This result is employed to derive the asymptotic scaling of the saddle spectral gap for the 3-spin in Sec. V.

Other useful asymptotic expressions for $\kappa \ll 1$ in the quantum region between the birth of the second minimum and classical phase transition point are

$$\frac{1}{\sigma_1} \approx \frac{1}{\sigma_*} = \sqrt{j} \left(\frac{x}{3} \right)^{1/4} \left(1 - \frac{9 - x^2}{8x^2} \kappa \right) + O(\kappa^2). \tag{C13}$$

The ratio deviates from unity only slightly:

$$\beta_2 = \frac{\sigma_1}{\sigma_*} = 1 - \frac{15}{8} x \kappa^2 + O(\kappa^3). \tag{C14}$$

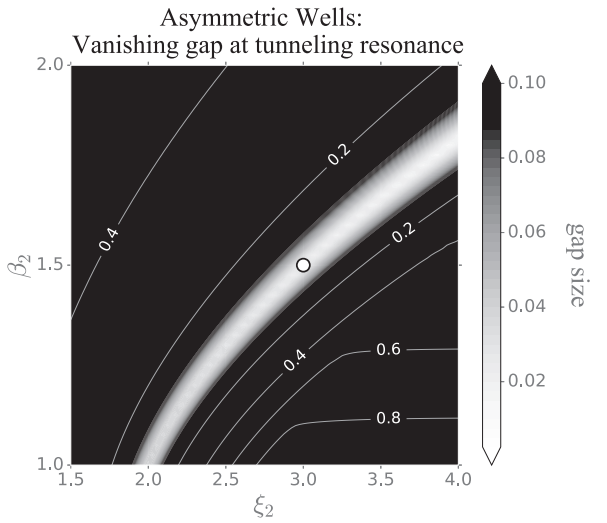

FIG. 19. Asymmetric double well: Here is illustrated the case that the left well is outside the Rayleigh boundary: $\{\xi_1, \beta_1\} \mapsto \{3.0, 1.5\}$ (white circle marker). Then one may employ WKB-like methods; the gap can become so small on resonance to be dictated by the potential shape and structure away from the parabolic extrema [20]. In such a case the piecewise-parabolic model loses its generality; errors or simplifications in the description of the potential have greater magnitude than the spectral gap calculated via this potential. The light-shaded channel identifies the resonance condition for $\{\xi_1, \beta_1, \xi_2, \beta_2\}$: an exponentially small minimum gap where one can expect a first-order phase transition via slow tunneling.

The scaled distance from the barrier summit to the ferromagnetic minimum is

$$\xi_2 = \frac{z_1 - z_*}{\sigma_*} = \sqrt{j}\left[\frac{x^{5/4}}{3^{1/4}}\kappa + O(\kappa^2)\right]. \tag{C15}$$

The remaining two parameters are

$$\xi_1 = \frac{z_*}{\sigma_*} = \sqrt{j}\left[\left(\frac{x}{3}\right)^{1/4}\left(\frac{3-x}{2}\right)\kappa + O(\kappa^2)\right], \tag{C16}$$

$$\beta_1 = \left(\frac{x}{3}\right)^{1/4} + O(\kappa). \tag{C17}$$

If we apply the ground-state resonance condition of Sec. IV to our scale-free model, this produces $x = 1$. Figure 4 presents the asymmetric well with $x = 1$. The parameters above then map onto Eq. (22) in the main text.

APPENDIX D: QUANTUM 2-SPIN: LIPKIN-MESHKOV-GLICK

The quantum 3-spin will prove challenging to implement experimentally. In contrast, the 2-spin, the simplest p-spin model, is an isotropic variant of the Lipkin-Meshkov-Glick (LMG) model introduced by Fallieros in 1959 in Ref. [12] to describe the nuclear physics of oxygen, and revisited by Lipkin and collaborators in Ref. [13]. It is an Ising model with infinite-range interactions; however, with 2-local rather than 3-local interactions the implementation on an experimental quantum annealer (such as that of Ref. [31]) may be relatively manageable. Current devices have up to $n = 4000$ qubits, but do not implement the fully connected graph required of the

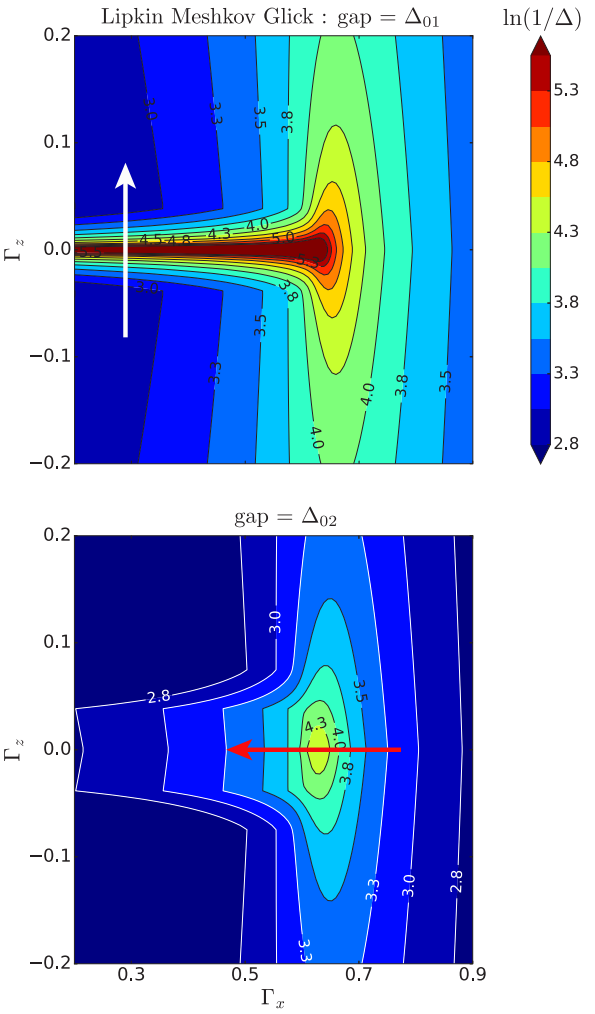

FIG. 20. The Lipkin-Meshkov-Glick (LMG) model with transverse and longitudinal field parameters Γ_x, Γ_z, respectively, exhibits the relatively gentle second-order phase transition we explored in Ref. [22] (lower plot). It occurs for an annealing schedule that follows the line of $\Gamma_z = 0$ from $\Gamma_x > 2/3$ to $\Gamma_x < 2/3$ (direction of red arrow). The minimum gap Δ_{02} near $\Gamma_z = 0, \Gamma_x = 2/3$ is polynomial in n; transitions between the ground and first excited state Δ_{01} are forbidden by parity along $\Gamma_z = 0$. In contrast, an annealing schedule for which $\Gamma_z \neq 0$ will not respect parity and the relevant gap is Δ_{01} (upper plot). A schedule crossing this zero longitudinal field line (direction of white arrow) must undergo a first-order phase transition if $\Gamma_x \lesssim 2/3$. Gap Δ_{01} is then exponentially small when crossing $\Gamma_z = 0$. The landscape above is for a $j = 25$ spin ensemble.

LMG model, (physical spins are topologically constrained to couple to nearby spins). Their partially connected architecture does, in fact, admit simulations of fully connected models of smaller ensembles, via a process called "embedding."

For LMG we dispense with the antiferromagnetic driver $+(1-\kappa)\hat{J}_x^2$. Instead there may exist some longitudinal field component in addition to the transverse one, represented by control parameters $\Gamma_{z,x}$, respectively:

$$\hat{H}_{\mathrm{LMG}} = -\Gamma_x\frac{\hat{J}_x}{j} - (1-\Gamma_x)\left[(1-|\Gamma_z|)\frac{\hat{J}_z^2}{j^2} + \Gamma_z\frac{\hat{J}_z}{j}\right]. \tag{D1}$$

We previously studied the behavior of this model during quantum annealing for the $\Gamma_z = 0$ setting [22]; it undergoes a second-order phase transition close to $\Gamma_x = 2/3$ where the unimodal ground state smoothly and continuously bifurcates into a bimodal Schrödinger cat state, eventually becoming a GHZ state [32]. The associated minimum gap at the phase transition is polynomially small. The symmetry of this model means that adiabatic transitions are forbidden from the ground to first excited state due to their opposite parity; the relevant minimum gap along the contour $\Gamma_z = 0$ in parameter space is actually $\Delta_{02} = E_2 - E_0 \sim n^{-4/3}$. For nonadiabatic (e.g., thermal) transitions $E_0 \mapsto E_1$, or the first-order annealing transitions where Γ_z is nonzero and switches sign, that gap also scales $\propto n^{-4/3}$ near $\Gamma_x \approx 2/3$ before becoming exponentially small in the tunnel-splitting limit characterized by the Gamow factor when $\Gamma_x \ll 2/3$. All of this is illustrated in the contour plots of Fig. 20.

The LMG continuous potential function becomes

$$V^{[\mathrm{LMG}]}(z) = -\sqrt{1-z^2} - \left(\frac{(1-|\Gamma_z|)z^2}{\gamma_x} + z\,\Gamma_z\right) + O(\hbar). \tag{D2}$$

For zero longitudinal field Γ_z and within the ferromagnetic phase $\Gamma_x < \Gamma_0$ the potential above is a beautifully symmetric double well, with a barrier height fully controlled by Γ_x. In terms of the ratio $\gamma_x = \Gamma_x/(1-\Gamma_x)$ the barrier is

$$V_0^{[\mathrm{LMG}]} = \frac{1}{\gamma_x} + \frac{\gamma_x}{4} - 1. \tag{D3}$$

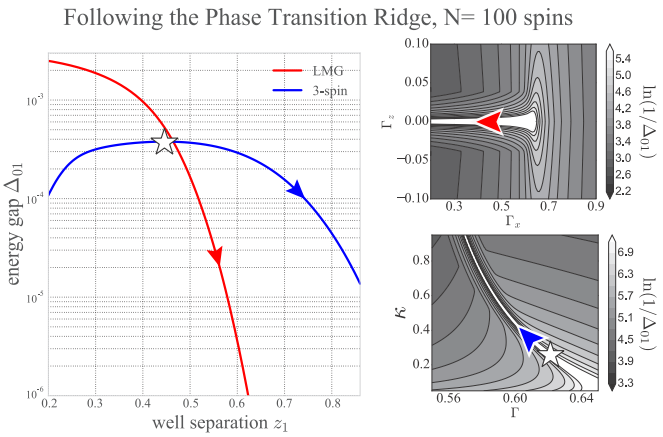

FIG. 21. For both the Lipkin-Meshkov-Glick (LMG; red curve) and quantum 3-spin model (blue curve), increasing the separation of the well minima z_1 leads to exponentially small minimum gaps, which occur along the "ridge" of the phase transition (contour plots to the right show these ridges in parameter space and the direction along which they are traversed as z_1 is increased). The 3-spin model is distinctive in that the minimum gap (blue) goes through a maximum in z_1, indicating a saddle point of "optimal catalysis" (white star marker). Exploring the ridge in the reversed direction now, from top left to bottom right (lower right panel), the well separation continues to decrease with decreasing κ, but the inverse mass $1/m \propto \kappa^2$. There is apparently a competition between the quantum "particle" becoming more confined at lower κ, but heavier at the same time. The increasing mass eventually wins at very low κ, causing the spectral gap to shrink again.

This very regular potential with a simple analytical form provides a perfect setting in which to examine the mechanism of vacuum delocalization. For γ_x increasing through the critical point $\gamma_x \mapsto \gamma_c = 2$, the potential barrier is completely razed to a flat-bottomed quartic profile $\sim z^4$ that evolves further into a single quadratic minimum centered at the origin $z = 0$ for $\gamma_x > 2$. The classical transition at $\gamma_x = 2$ is described by a green contour line in the right-side plots of Fig. 6. In the small-γ_x ferromagnetic phase (double-well potential) one may introduce asymmetry or bias in the potential by a (positive or negative) longitudinal field of $|\Gamma_z| \ll 1$. This will lower one well minimum with respect to the other and the adiabatic ground state will lose its fragile superposition state. It shifts completely to being a spin-coherent state pointed at the deeper well.

Then by reversing the bias of Γ_z the ground state will have to tunnel across the large intervening barrier from the false minimum to the true minimum. A magnetization mea-

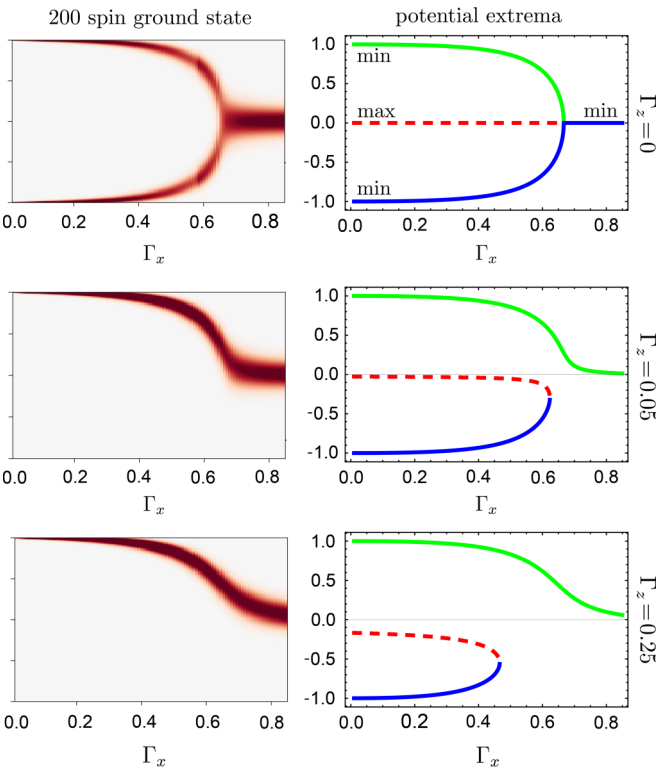

FIG. 22. For longitudinal field $\Gamma_z \mapsto \{0, +0.05, +0.25\}$ the ground-state amplitude density (found numerically) and potential extrema (derived analytically) are shown in the left and right columns, respectively. For the right column, the locus of the potential maxima in coordinate space z is indicated (dashed red line), with the exterior minima shown in blue (shallow) and green (deep). As the barrier maximum is lowered with increasing Γ_x, for a symmetry-breaking $\Gamma_z > 0$ one of the minima collides with the now off-center maximum. Only the green minimum remains, moving towards the origin $z = 0$ as Γ_x is increased further. Changing Γ_z to $-\Gamma_z$ just reflects the diagrams through the origin (top to bottom). In the lower figure then the minimum at $z \approx -1$ would become the true minimum, and the (now false) ground state at $z = +1$ will tunnel through the intervening barrier (red dashed maximum line), unless the barrier is small enough, Eq. (D3), for vacuum delocalization to occur.

surement should be able to record the characteristic time for the population inversion to occur. The shape of the phase transition ridge for the LMG model is compared with that of the 3-spin in Fig. 21, and the extrema of the LMG potential energy are plotted in Fig. 22.

When γ_x is increased to lower the intervening barrier to a fixed height (the analog of nonstoquastic catalysis in the p-spin model), one may observe directly a crossover in the characteristic magnetization "switching time" (population transfer from the left to the right well) as Γ_z is varied from slightly negative to slightly positive. Increasing the transverse field, the $\gamma_x \lesssim 2$ or $\Gamma_x \lesssim 2/3$ regime (wells start to coalesce as the potential barrier between them shrinks) should permit a polynomial gap for a range of Γ_x, allowing the ground-state energy to delocalize close to the barrier summit, before the wells completely coalesce at $\Gamma_x = 2/3$. The change in the rate of population inversion from exponentially slow to rapid polynomial timescales should be apparent and measurable in the $\Gamma_x \lesssim 2/3$ regime. Because parameter $1/j$ plays the role of an effective $\hbar$ when transforming to a particle in a potential, smaller ensembles exhibit more "extravagantly" quantum effects, e.g., magnified vacuum energies, allowing increased mobility across barriers without (exponentially slow) tunneling.

[1] T. Kadowaki and H. Nishimori, Quantum annealing in the transverse Ising model, Phys. Rev. E **58**, 5355 (1998).

[2] E. Farhi, J. Goldstone, S. Gutmann, and M. Sipser, Quantum computation by adiabatic evolution, arXiv:quant-ph/0001106.

[3] M. Born and V. Fock, Beweis des adiabatensatzes, Z. Phys. **51**, 165 (1928).

[4] G. Gamow, Zur quantentheorie des atomkernes (on the quantum theory of the atomic nucleus), Z. Phys. A **51**, 204 (1928).

[5] T. Jörg, F. Krzakala, J. Kurchan, A. C. Maggs, and J. Pujos, Energy gaps in quantum first-order mean-field–like transitions: The problems that quantum annealing cannot solve, Europhys. Lett. **89**, 40004 (2010).

[6] A. Bulatov and V. Smelyanskiy, Total suppression of a large spin tunneling barrier in quantum adiabatic computation, arXiv:quant-ph/0208189.

[7] Y. Seki and H. Nishimori, Quantum annealing with antiferromagnetic fluctuations, Phys. Rev. E **85**, 051112 (2012).

[8] L. Hormozi, E. W. Brown, G. Carleo, and M. Troyer, Nonstoquastic Hamiltonians and quantum annealing of an Ising spin glass, Phys. Rev. B **95**, 184416 (2017).

[9] D. Jonathan and M. B. Plenio, Entanglement-Assisted Local Manipulation of Pure Quantum States, Phys. Rev. Lett. **83**, 3566 (1999).

[10] T. Albash and D. A. Lidar, Adiabatic quantum computation, Rev. Mod. Phys. **90**, 015002 (2018).

[11] L. Rayleigh, XXXI. Investigations in optics, with special reference to the spectroscope, London Edinburgh Dublin Philos. Mag. J. Sci. **8**, 261 (1879).

[12] S. Fallieros, Collective oscillations in oxygen-16, Ph.D. thesis, University of Maryland, College Park, 1959.

[13] H. J. Lipkin, N. Meshkov, and A. Glick, Validity of many-body approximation methods for a solvable model. I. Exact solutions and perturbation theory, Nucl. Phys. **62**, 188 (1965).

[14] J. Zhang *et al.*, Observation of a many-body dynamical phase transition with a 53-qubit quantum simulator, Nature (London) **551**, 601 (2017).

[15] A. Zettl, *Sturm-Liouville Theory* (American Mathematical Society, Providence, RI, 2010).

[16] An additional assumption is that the energy scales of the doublets versus the interdoublet spacing are large enough that confining analysis to the two-state subspace is justified. This assumption becomes invalid for wells that are closer together; the overlap between the localized oscillators becomes appreciable, and the intradoublet and interdoublet level spacings become comparable, as on the left side of Fig. 1. Then a different argument will be needed to relate the spectral gap to the rate of migration across the barrier. The orthonormal basis of eigenfunctions is no longer composed of symmetrized Gaussians, but parabolic cylinder functions with real and imaginary arguments.

[17] A. Garg, Tunnel splittings for one-dimensional potential wells revisited, Am. J. Phys. **68**, 430 (2000).

[18] J. Connor, On the analytical description of resonance tunneling reactions, Mol. Phys. **15**, 37 (1968).

[19] S. M. Halataei and A. J. Leggett, Tunnel splitting in asymmetric double well potentials: An improved WKB calculation, arXiv:1703.05758.

[20] E. V. Vybornyi, Tunnel splitting of the spectrum and bilocalization of eigenfunctions in an asymmetric double well, Theor. Math. Phys. **178**, 93 (2014).

[21] G. Rastelli, Semiclassical formula for quantum tunneling in asymmetric double-well potentials, Phys. Rev. A **86**, 012106 (2012).

[22] G. A. Durkin, Asymptotically optimal probes for noisy interferometry via quantum annealing to criticality, Phys. Rev. A **94**, 043821 (2016).

[23] R. K. Mains, I. Mehdi, and G. I. Haddad, Effect of spatially variable effective mass on static and dynamic properties of resonant tunneling devices, Appl. Phys. Lett. **55**, 2631 (1989).

[24] B. Gönül, O. Özer, B. Gönül, and F. Üzgün, Exact solutions of effective-mass Schrödinger equations, Mod. Phys. Lett. A **17**, 2453 (2002).

[25] J. Tsuda, Y. Yamanaka, and H. Nishimori, Energy gap at first-order quantum phase transitions: An anomalous case, J. Phys. Soc. Jpn. **82**, 114004 (2013).

[26] H. Nishimori and K. Takada, Exponential enhancement of the efficiency of quantum annealing by non-stochastic Hamiltonians, Front. ICT **4**, 2 (2017).

[27] W. Van Dam, M. Mosca, and U. Vazirani, How powerful is adiabatic quantum computation? in *Proceedings of the 2001 IEEE International Conference on Cluster Computing* (IEEE, New York, 2001), pp. 279–287.

[28] E. W. Dijkstra, A note on two problems in connexion with graphs, Numer. Math. **1**, 269 (1959).

[29] K. W. Ford, D. L. Hill, M. Wakano, and J. A. Wheeler, Quantum effects near a barrier maximum, Ann. Phys. **7**, 239 (1959).

[30] E. Merzbacher, in *Quantum Mechanics*, 2nd ed. (Wiley, Hoboken, NJ, 1970), Chap. 6, pp. 68–76.

[31] M. Johnson *et al.*, Quantum annealing with manufactured spins, Nature (London) **473**, 194 (2011).

[32] D. M. Greenberger, M. A. Horne, and A. Zeilinger, Going beyond Bell's theorem, in *Bell's Theorem, Quantum Theory and Conceptions of the Universe* (Springer, Berlin, 1989), pp. 69–72.